Scale-up Analysis of Continuous Cross-flow Atomic Layer Deposition Reactor Designs

Holmqvist, Anders; Magnusson, Fredrik; Stenström, Stig

Published in:
Chemical Engineering Science

DOI:
10.1016/j.ces.2014.07.002

2014

Document Version:
Peer reviewed version (aka post-print)

Scale-up Analysis of Continuous Cross-flow Atomic Layer Deposition Reactor Designs

A. Holmqvist[a,*], F. Magnusson[b], S. Stenström[a]

[a] *Department of Chemical Engineering, Lund University, P.O. Box 124, SE-221 00 Lund, Sweden*
[b] *Department of Automatic Control, Lund University, P.O. Box 118, SE-221 00 Lund, Sweden*

Abstract

This paper presents the development of a non-dimensional model of a continuous cross-flow atomic layer deposition (ALD) reactor with temporally separated precursor pulsing and a structured model-based methodology for scaling up the substrate dimensions. The model incorporates an ALD gas–surface reaction kinetic mechanism for the deposition of thin ZnO films from $Zn(C_2H_5)_2$ and H_2O precursors that was experimentally validated in our previous work (Holmqvist et al., 2012, 2013a). In order to maintain dynamic similarity, a scaling analysis was applied based on the dimensionless numbers, appearing in non-dimensionalized momentum and species mass conservation equations, that describe the convective laminar flow, mass transfer and heterogeneous reaction. The impact on these dimensionless numbers and, more importantly, the impact on the limit-cycle deposition rate and its relative uniformity was thoroughly investigated when linearly scaling up the substrate dimensions. In the scale-up procedure, the limit-cycle precursor utilization was maximized by means of dynamic optimization, while ensuring that identical deposition profiles were obtained in the scaled-up system. The results presented here demonstrated that the maximum precursor yields were promoted at higher substrate dimen-

*Corresponding author. Tel.: +46 46 222 4925; fax: +46 46 222 4526
Email addresses: anders.holmqvist@chemeng.lth.se (A. Holmqvist), fredrik.magnusson@control.lth.se (F. Magnusson), stig.stenstrom@chemeng.lth.se (S. Stenström)

sions. Limit-cycle dynamic solutions to the non-dimensionalized model, computed with a collocation discretization in time, revealed that it is a combination of the degree of precursor depletion in the flow direction and the magnitude of the pressure drop across the reactor chamber that governs the extent of the deposition profile non-uniformity. A key finding of this study is the identification of optimal scaling rules for maximizing precursor utilization in the scaled-up system while maintaining fixed absolute growth rate and its relative uniformity.
Keywords: Atomic layer deposition, Scale-up analysis, Dynamic optimization, Mathematical modeling, Limit-cycle kinetics, Numerical analysis

1. Introduction

Atomic layer deposition (ALD) is a gas-phase deposition process that can produce conformal thin films with controlled uniform thickness in the nanometer range (George, 2010). This attribute is inherent to the sequential self-terminating (Puurunen, 2005) ALD gas–surface reactions (Masel, 1996), in which the non-overlapping alternating injection of chemical precursor species separated by intermediate purge steps prevents reactions in the gas phase (Miikkulainen et al., 2013). The deposition process depends strongly on two characteristic time scales (see, for example, (Adomaitis, 2010; Granneman et al., 2007)): the time scale of underlying reactor-scale mass transport (Aarik et al., 2006; Jur and Parsons, 2011; Mousa et al., 2012), and the time scale of the heterogeneous gas–surface reactions (Ritala and Leskelä, 2002; Yanguas-Gil and Elam, 2014).

Conventional thermal ALD is a special modification of the chemical vapor deposition (CVD) technique. One of the essential advantages of ALD is that its self-terminating nature enables uniform coating of substrates with large surface areas (Levy and Nelson, 2012; Sundaram et al., 2010), and it is thus easier to scale up the process of ALD than that of CVD (Yanguas-Gil and Elam, 2012). In this study, the geometrical scale up of the substrate dimensions in cross-flow, low-volume ALD reactor designs with temporal precursor pulsing was

investigated. Such reactor designs are of major interest for the equipment used to manufacture substrates of large surface area (Henn-Lecordier et al., 2011). Such substrates are subject to stringent uniformity constraints (Cleveland et al., 2012), where the fundamental requirement for growth uniformity is the attainment of surface saturation. This, in turn, requires adequate precursor delivery (Knoops et al., 2011; Ylilammi, 1995), optimal process operating conditions, and optimal reactor design (Elers et al., 2006). Non-uniform film thickness profiles in cross-flow ALD reactor designs can result from precursor depletion, which can be a concern for precursors with a low vapor pressure (Granneman et al., 2007).

Several studies on scaling up horizontal reactor designs for CVD have been published, (see, for example, Dam et al. (2007) and the references cited therein). However, a model-based study of dimensionless numbers with respect to scaling up has never been rigorously carried out for ALD growth. The overall objective of the present study, therefore, was to develop a model-based method for the geometrical scale up of the substrate dimension in cross-flow reactor designs that use temporal precursor pulsing. The scale-up procedure provides a fixed absolute growth rate and relative uniformity while maximizing precursor utilization. This methodology was applied to an experimentally validated mechanism of the ALD gas–surface reactions for the deposition of thin ZnO films from $Zn(C_2H_5)_2$ and H_2O precursors (Holmqvist et al., 2012, 2013a). The study presented here had three main objectives:

i) To develop a structured model-based method for the geometrical scaling up of the substrate dimensions in continuous cross-flow ALD reactor designs, and to identify the scaling guidelines that are best suited to maintaining the limit-cycle deposition rate and its relative uniformity in the scaled-up system.

ii) To investigate dynamic similarity by deriving the fully coupled compressible flow equations, along with their boundary conditions and initial conditions, of the developed reactor model in its non-dimensional form.

iii) To formulate and solve a dynamic optimization problem in order to optimize precursor utilization, subject to terminal constraints of the limit-cycle deposition rate and its relative uniformity.

This paper is organized as follows: Section 2 outlines the mechanism of the ZnO ALD gas–surface reactions. Section 3 derives the non-dimensional ALD reactor model and identifies the associated non-dimensional variables that appear. Section 4 describes the scale-up strategies and formulates the dynamic optimization problem, while Section 5 outlines the modeling and optimization framework. Section 6 presents the results from the scale-up analysis, and Section 7 presents concluding remarks.

1.1. Previous Modeling

Our previous work (Holmqvist et al., 2012, 2013a,b), which presents a mechanistic model of the continuous cross-flow ALD reactor system F-120 manufactured by ASM Microchemistry Ltd. (Suntola, 1992), is particularly relevant to the present article. The work of Yanguas-Gil and Elam (2012) on what is known as the "SMART" model (where "SMART" is an acronym for "Simple Model for Atomic layer deposition precursor Reaction and Transport") for the analysis of transport-reaction processes in a tubular, laminar flow reactor is also highly relevant. The non-dimensional model presented in the present study is founded on the dimensional model that we have previously developed (Holmqvist et al., 2012, 2013a,b), and the approximation of fully developed laminar channel flow defined in a one-dimensional computational domain. Moreover, the model presented here comprises fully coupled compressible equations for the conservation of mass, momentum and individual gas-phase species, while the SMART model, in contrast, assumes incompressible flow. The application range of the model is expanded in this way to include the region in which the pressure of the precursor is significant, relative to that of the carrier gas, which is necessary in the scale-up analysis.

2. ALD Surface Reaction Kinetics

The predictive capability of the developed physically-based model to decouple the effects of precursor partial pressure, exposure times, process manipulated variables, and the dynamics of each exposure period on the limit-cycle spatially dependent substrate film thickness profile is essential for the purposes of this investigation. For this reason, an experimentally validated gas–surface reaction mechanism for the deposition of ZnO films from $Zn(C_2H_5)_2$ and H_2O precursors was incorporated into the model developed during the present study, in order to obtain as accurate a model as possible. The experimental investigation was conducted in the F-120 reactor system from ASM Microchemistry Ltd. (Suntola, 1992) and the estimated rate coefficients from *ex situ* X-ray reflectivity (XRR) thickness profile measurements are reported in Holmqvist et al. (2013a), which contains also details of the film characterization and data preprocessing.

Consider a simple ZnO ALD gas–surface reaction kinetic mechanism, with the overall reaction stoichiometry given by:

$$Zn(C_2H_5)_2 + H_2O \longrightarrow ZnO + 2C_2H_6 \tag{R1}$$

and only encompassing the primary irreversible and sequential elementary gas–surface reactions for the $Zn(C_2H_5)_2$ and H_2O precursors on a normally hydroxylated surface. Such a reactions were defined in Holmqvist et al. (2013a) as:

$$\nu(-OH)\langle s\rangle + Zn(C_2H_5)_2\langle g\rangle \xrightarrow{k_1^{fwd}} (-O-)_\nu Zn(C_2H_5)_{2-\nu}\langle s\rangle + \nu C_2H_6\langle g\rangle \tag{R2a}$$

$$(-O-)_\nu Zn(C_2H_5)_{2-\nu}\langle s\rangle + H_2O\langle g\rangle \xrightarrow{k_2^{fwd}} (-O-)Zn(-OH)_\nu\langle s\rangle + (2-\nu)C_2H_6\langle g\rangle \tag{R2b}$$

Here $\langle s\rangle$ and $\langle g\rangle$ denote surface and gaseous species, respectively, and $\nu = 1.37$ (Elam and George, 2003) is the average number of hydroxyl groups that react with each $Zn(C_2H_5)_2$ molecule. Thus, the ZnO deposition half-reactions (Reactions (R2a and R2b)) were not broken down further into the elemental

Table 1: A summary of gaseous and fractional surface coverage species in Reactions (R2a–R2d), and their abbreviations.

Gaseous species ($\langle g \rangle$)	α	Surface species ($\langle s \rangle$)	κ
$Zn(C_2H_5)_2$	A	$(-OH)$	$A*$
H_2O	B	$(-O-)_\nu Zn(C_2H_5)_{2-\nu}$	$B*$
C_2H_6	C	$(-O)$	$C*$
N_2	P		

adsorption and reaction steps during each precursor exposure (as is done in, for example, Elliott (2012); Ren (2009); Travis and Adomaitis (2013a,b,c)). Thereby, the ligand elimination was assumed to proceed without intermediate adsorption adducts or their transition states being formed, and that this is the rate-limiting step.

The irreversible half-reactions defined in Reaction (R2) subject to constant activation energies govern a *growth per cycle* (GPC) that increases strictly with the deposition temperature, and hence, Reaction (R2) cannot describe the sharp decrease in GPC that occurs at elevated temperatures (see, for example, Yousfi et al. (2000)). This phenomenon is generally attributed to the gradual reduction of the surface hydroxyl groups through the recombination reaction (Reaction (R2c)) (Deminsky et al., 2004; Matero et al., 2000; Rahtu et al., 2001):

$$2(-OH)\langle s \rangle \xrightarrow{k_3^{\text{rev}}} (-O)\langle s \rangle + H_2O\langle g \rangle \tag{R2c}$$

$$(-O)\langle s \rangle + H_2O\langle g \rangle \xrightarrow{k_4^{\text{fwd}}} 2(-OH)\langle s \rangle \tag{R2d}$$

where the hydroxyl groups may be reformed on the oxide surface during exposure to H_2O through the reverse reaction (Reaction (R2d)). It is, however, noteworthy that the GPC that is obtained, which is governed by the limit-cycle ZnO ALD kinetics proposed in Reactions (R2), has a convex temperature dependence. Finally, the abbreviations for the gaseous and fractional surface species in Reactions (R2a–R2d) used in this paper are listed in Table 1.

3. Physical Modeling

A one-dimensional representation of the square duct reaction chamber (with dimensions ($L \times W \times H$) $5.0 \times 5.0 \times 0.2$ (cm)) of the reactor system constituted the spatial domain, $z \in [0, L]$, in the present study, with its z-axis coincident with the flow direction. Further details of the reactor system are given in Holmqvist et al. (2012, 2013b) and in Baunemann (2006); Yousfi et al. (2000). The original experimental configuration is denoted as the *Reactor* $\mathscr{A}$ in the following scale-up analysis.

3.1. Nominal State and Algebraic Variables

For this paper a non-dimensionalized, physically-based model was used to calculate the spatially and temporally dependent concentration and deposition profiles for the original *Reactor* $\mathscr{A}$ and have subsequent been applied to the scaled-up *Reactor* $\mathscr{B}$, while keeping certain dimensionless numbers in the differential equations and boundary conditions the same for both systems. In this way, the scale-up method strives to preserve dynamic similarity. However, in order to maintain constant dimensionless numbers, the underlying nominal state and algebraic variables $[\hat{\rho}, \hat{v}_\zeta, \hat{w}_\alpha, \hat{p}]$ must be expressed in terms of the process manipulated variables, $\mathbf{u} = [\dot{Q}_\beta, \dot{V}_{\mathrm{VP}}, \dot{Q}_\alpha, \Delta\tau_\alpha]$ and $\forall\alpha \in \{A, B\}$. Thus, the length, $\zeta \in [\zeta_0, \zeta_{\mathrm{end}}]$, and time, $\tau \in [\tau_0, \tau_f]$, are scaled by the nominal values L and $L/\hat{v}_\zeta$, respectively. Additionally, the nominal mass averaged velocity, $\hat{v}_\zeta$, density, $\hat{\rho}$, and pressure, $\hat{p}$, of the carrier gas as well as the nominal precursor mass fraction, $\hat{\omega}_\alpha$, are conveniently expressed by the reactor dynamic material balances of the continuous stirred-tank reactor (CSTR) model:

$$\left[\!\left[\frac{\hat{v}_\zeta}{L}\right]\!\right]\frac{d\hat{\rho}}{d\tau} = \frac{1}{V}\sum_{\forall\alpha}\dot{Q}_\alpha\rho_{\mathrm{STP},\alpha}\Pi_\alpha(\tau,\Delta\tau_\alpha) - \frac{\dot{V}_{\mathrm{VP}}}{V}\hat{\rho} + \sum_{\forall\alpha}S_\alpha \tag{1a}$$

$$\left[\!\left[\frac{\hat{v}_\zeta}{L}\right]\!\right]\frac{d\hat{\rho}\hat{\omega}_\alpha}{d\tau} = \frac{1}{V}\dot{Q}_\alpha\rho_{\mathrm{STP},\alpha}\Pi_\alpha(\tau,\Delta\tau_\alpha) - \frac{\dot{V}_{\mathrm{VP}}}{V}\hat{\rho}\hat{\omega}_\alpha + S_\alpha \tag{1b}$$

where S_α denotes the net mass consumption owing to the heterogeneous gas–surface reactions (see Section 2). See Travis and Adomaitis (2013a) for further details of how the reactor dynamic material balances are derived.

A smooth rectangular function was used to model the non-overlapping precursor injections in a cyclic time sequence. This function, $\Pi_\alpha(\tau, \Delta\tau_\alpha) \in [0, 1]$, was composed of superposed continuously differentiable logistic functions, $L(\tau)$:

$$\Pi_\alpha(\tau, \Delta\tau_\alpha) = L(\bar{\tau} - \bar{\tau}_{0,\alpha}) - L(\bar{\tau} - \bar{\tau}_{f,\alpha}) \tag{2a}$$

$$L(\bar{\tau}) = [1 + \exp(-\delta\tau_\alpha \bar{\tau})]^{-1} \tag{2b}$$

where $\bar{\tau} = N_{\Delta\tau} - \lfloor N_{\Delta\tau} \rfloor$ is the normalized cycle time, $N_{\Delta\tau} = \tau/\Delta\tau$ is the cycle number, $\Delta\tau = \Delta\tau_A + \Delta\tau_B + 2\Delta\tau_P$ denotes a complete ALD cycle, $\delta\tau_\alpha$ is a parameter that influences the maximum derivative of the function, and $\Delta\tau_\alpha = (\bar{\tau}_{f,\alpha} - \bar{\tau}_{0,\alpha})\Delta\tau$. Imposing stationarity on Eq. (1) under non-reactive conditions, i.e. prescribing $S_\alpha := 0$, allows to define the following explicit relationships:

$$\hat{\rho} := \frac{\dot{Q}_\beta \rho_{\mathrm{STP},\beta}}{\dot{V}_{\mathrm{VP}}} \tag{3a}$$

$$\hat{\omega}_\alpha := \frac{\dot{Q}_\alpha \rho_{\mathrm{STP},\alpha}}{\dot{Q}_\alpha \rho_{\mathrm{STP},\alpha} + \dot{Q}_\beta \rho_{\mathrm{STP},\beta}} \tag{3b}$$

The nominal density, $\hat{\rho}$, in Eq. (3a) is defined for the carrier gas purge by prescribing $\Pi_\alpha(\tau, \Delta\tau_\alpha) := 0$, whereas the nominal gas-phase mass fraction, $\hat{\omega}_\alpha$, in Eq. (3b) is defined for the precursor pulse by prescribing $\Pi_\alpha(\tau, \Delta\tau_\alpha) := 1$ and $\forall\alpha \in \{A, B\}$. Likewise, $\hat{p}$ and $\hat{v}_\zeta$ are defined for the carrier gas purge by means of the equation of state, where:

$$\hat{p} = \frac{\hat{\rho}}{M_\beta} RT := \frac{1}{\dot{V}_{\mathrm{VP}}} \frac{\dot{Q}_\beta \rho_{\mathrm{STP},\beta}}{M_\beta} RT \tag{3c}$$

$$\hat{v}_\zeta := \frac{1}{A'} \frac{\dot{Q}_\beta \rho_{\mathrm{STP},\beta}}{M_\beta} RT \frac{1}{\hat{p}} := \frac{\dot{V}_{\mathrm{VP}}}{A'} \tag{3d}$$

where $\rho_{\mathrm{STP},\beta}$ is the density of the carrier gas species β at standard temperature and pressure (STP).

It is noteworthy that the CSTR model was exploited in this study due to its inherent formalism, which describes the correlation between the mass flow of the αth precursor, $\dot{Q}_\alpha$, and that of the carrier gas, $\dot{Q}_\beta$, (which are both specified upstream of the reaction chamber), and the volumetric flow rate through the vacuum pump, $\dot{V}_{\mathrm{VP}}$, (which is specified downstream of the reaction chamber).

Accordingly, the CSTR model conveniently correlates the impact of the free design variables, $\mathbf{u}$, on the nominal state and algebraic variables needed to derive the equations that describe the spatially distributed reactor model in its non-dimensional form. The non-dimensionalized spatially distributed reactor model was subsequent utilized in the scale-up analysis.

3.2. Spatially Distributed ALD Reactor Model

The isothermal and variable-density gas flow in the viscous regime can be described by fully coupled, compressible (Bird et al., 1960) equations for the conservation of mass, momentum, and individual gas-phase species. This is the type of gas flow encountered in low-volume, continuous cross-flow ALD reactor designs with temporal precursor pulsing. The governing equations defined in the non-dimensionalized spatial, $\zeta \in [\zeta_0, \zeta_{\text{end}}]$, and temporal, $\tau \in [\tau_0, \tau_f]$, domains are, in an appropriate non-dimensional form:

$$\frac{\partial \rho}{\partial \tau} = -\frac{\partial}{\partial \zeta}\Big(\rho v_\zeta\Big) + \sum_{\forall \alpha} \Big[\!\Big[\frac{L}{\hat{\rho}\hat{v}_\zeta \hat{\omega}_\alpha} \Big]\!\Big] S_\alpha \tag{4}$$

$$\frac{\partial \rho v_\zeta}{\partial \tau} = -\frac{\partial}{\partial \zeta}\Big(\rho v_\zeta v_\zeta + \mathscr{P}\Big) + \Big[\!\Big[\frac{\hat{\mu}}{\hat{\rho}\hat{v}_\zeta L} \Big]\!\Big] \frac{4}{3} \frac{\partial}{\partial \zeta}\Big(\mu \frac{\partial v_\zeta}{\partial \zeta}\Big) - \Big[\!\Big[\frac{\hat{\mu}}{\hat{\rho}\hat{v}_\zeta L} \Big]\!\Big] \Phi_\zeta \tag{5}$$

$$\frac{\partial \rho \omega_\alpha}{\partial \tau} = -\frac{\partial}{\partial \zeta}\Big(\rho v_\zeta \omega_\alpha\Big) + \Big[\!\Big[\frac{\hat{\mathscr{D}}_{\alpha\beta}}{\hat{v}_\zeta L} \Big]\!\Big] \frac{\partial}{\partial \zeta}\Big(\rho \mathscr{D}_{\alpha\beta} \frac{\partial \omega_\alpha}{\partial \zeta}\Big) + \Big[\!\Big[\frac{L}{\hat{\rho}\hat{v}_\zeta \hat{\omega}_\alpha} \Big]\!\Big] S_\alpha \tag{6}$$

where $\mathscr{P} = p[\![\hat{p}/(\hat{\rho}\hat{v}_\zeta \hat{v}_\zeta)]\!]$ denotes the characteristic modified pressure. Two dimensionless numbers dominate the gas flow and mass transfer:

$$\text{Re} := \Big[\!\Big[\frac{\hat{\rho}\hat{v}_\zeta L}{\hat{\mu}} \Big]\!\Big] \tag{7}$$

$$\text{Pe} := \Big[\!\Big[\frac{\hat{v}_\zeta L}{\hat{\mathscr{D}}_{\alpha\beta}} \Big]\!\Big] \tag{8}$$

where Re is the Reynolds number, which describes the ratio between the inertial forces and the viscous forces, and Pe is the Peclet number, which describes the ratio between the convective mass transport and the diffusive mass transport. Here, ρ and μ are the non-dimensional density and the dynamic viscosity of the gas mixture at a certain nominal pressure and temperature. The non-dimensional pressure, p, is governed by the equation of state, and (making use

of Eq. (3a)) is given by:

$$p = \Big(\frac{\hat{\rho}}{\hat{p}}RT\Big)\rho\sum_{\forall\alpha}\frac{\hat{\omega}_\alpha\omega_\alpha}{M_\alpha} \tag{9}$$
$$:= \rho\sum_{\forall\alpha}\Big(\hat{\omega}_\alpha\frac{M_\beta}{M_\alpha}\Big)\omega_\alpha$$

The non-dimensional transport coefficients, $\mathscr{D}_{\alpha\beta}$ and μ_α, in Eqs. (4–8) were determined from the Chapman-Enskog kinetic theory of dilute gases (Hirschfelder et al., 1964; Reid et al., 1988), and the non-dimensional viscosity for the multicomponent mixture of gases, μ, was determined from the semi-empirical mixing formula (Wilke, 1950). The transport coefficients were converted to non-dimensional forms by determining the corresponding values at the aforementioned nominal values determined by Eq. (3). Finally, the last term in Eq. (5) is given by:

$$\Phi_\zeta = 12(L/H)^2\mu v_\zeta \tag{10}$$

and originates from the shear stress, $-\mu\partial v_\zeta(y)/\partial y$, and has been derived by assuming that the flow in a square duct is fully developed and laminar, with a velocity distribution given by $v_\zeta(y) = v_{\zeta,\max}(1-[2y/H]^2)$, with $y \in (H/2)[-1,1]$ and $v_{\zeta,\max} = (3/2)v_\zeta$ (Bird et al., 1960).

3.2.1. Boundary Conditions

Analogous to inlet and outlet flow rates of the CSTR model (see Eqs. (1 and 3)), the boundary conditions to the set of partial differential equations (PDEs) (Eqs. (4–6)) prescribes the precursor and carrier gas mass flow as a standard volumetric flow rate at the inlet, and the volumetric flow rate through the vacuum pump, $\dot{V}_{\mathrm{VP}}$, at the outlet. Thus, the inlet, $\zeta = \zeta_0$, mass fluxes for each component α and for the gas mixture, along with a Neumann condition on

the velocity, are given by the equations:

$$(\rho v_\zeta)\Big|_{\zeta=\zeta_0} = \frac{1}{\hat{\rho}\hat{v}_\zeta}\frac{1}{A'}\sum_{\forall\alpha}\dot{Q}_\alpha\rho_{\mathrm{STP},\alpha}\Pi_\alpha(\tau,\Delta\tau_\alpha) \tag{11}$$

$$\frac{\partial v_\zeta}{\partial\zeta}\Big|_{\zeta=\zeta_0} = 0 \tag{12}$$

$$(\rho v_\zeta\omega_\alpha)\Big|_{\zeta=\zeta_0} = \frac{1}{\hat{\rho}\hat{v}_\zeta\hat{\omega}_\alpha}\frac{1}{A'}\dot{Q}_\alpha\rho_{\mathrm{STP},\alpha}\Pi_\alpha(\tau,\Delta\tau_\alpha) \tag{13}$$

Further, the outlet boundary condition, $\zeta = \zeta_{\mathrm{end}}$, prescribes that the diffusive mass is zero along with a Dirichlet condition on the velocity:

$$v_\zeta\Big|_{\zeta=\zeta_{\mathrm{end}}} = \frac{1}{\hat{v}_\zeta}\frac{\dot{V}_{\mathrm{VP}}}{A'} \tag{14}$$

$$\frac{\partial\omega_\alpha}{\partial\zeta}\Big|_{\zeta=\zeta_{\mathrm{end}}} = 0 \tag{15}$$

3.3. Gas-phase Species Flux at the Growth Surface

The heterogeneous ALD gas–surface reactions (Reaction (R2)) lead to a net mass consumption at the substrate surface. The molar reaction rate of the ith elementary reaction is described by the general reversible Langmuir formalism (Holmqvist et al., 2012):

$$r_i = \left[\!\!\left[\frac{\hat{\rho}\hat{\omega}_\alpha}{M_\alpha}RT\right]\!\!\right]\rho\omega_\alpha k_i^{\mathrm{fwd}}\Lambda^{n_i^{\mathrm{fwd}}}\Big(1-\sum_{\forall\ell}\theta_\ell\Big)^{n_i^{\mathrm{fwd}}} - k_i^{\mathrm{rev}}\Lambda^{n_i^{\mathrm{rev}}}\theta_\kappa^{n_i^{\mathrm{rev}}} \tag{16}$$

where Λ is the maximum molar concentration of surface sites per unit area available for deposition, the subscript ℓ represents all κth surface species with which the αth gaseous species cannot undergo a reaction, and n_i^{fwd} and n_i^{rev} are the orders of the forward and reverse reactions, respectively. The partial pressure, p_α, of the αth precursor in Eq. (16) can be expressed in terms of the mass fraction, ω_α, and the density of the gas mixture, ρ, using the equation of state, to give:

$$\hat{p}_\alpha p_\alpha := \left[\!\!\left[\frac{\hat{\rho}\hat{\omega}_\alpha}{M_\alpha}RT\right]\!\!\right]\rho\omega_\alpha \tag{17}$$

Consequently, the source term, S_α, in the species-continuity equation (Eq. (6)) states that the total gas-phase mass flux of the αth species at the growth surface

is balanced by the net consumption or production of mass per unit area:

$$\Big[\!\Big[\frac{L}{\hat{\rho}\hat{v}_\zeta\hat{\omega}_\alpha}\Big]\!\Big] S_\alpha = \Big[\!\Big[\frac{L}{\hat{\rho}\hat{v}_\zeta\hat{\omega}_\alpha}\Big]\!\Big]\Big(\frac{A}{V}\Big) M_\alpha \sum_{i=1}^{N_i} \xi_{\alpha,i} r_i \tag{18}$$

$$:= \sum_{i=1}^{N_i} \xi_{\alpha,i} \Big[\Big[\!\Big[\frac{L}{\hat{v}_\zeta}\Big(\frac{A}{V}\Big) RT k_i^{\mathrm{fwd}} \Lambda^{n_i^{\mathrm{fwd}}}\Big]\!\Big] \rho\omega_\alpha \Big(1 - \sum_{\forall \ell} \theta_\ell\Big)^{n_i^{\mathrm{fwd}}} - \Big[\!\Big[\frac{L}{\hat{v}_\zeta}\frac{M_\alpha}{\hat{\rho}\hat{\omega}_\alpha}\Big(\frac{A}{V}\Big) k_i^{\mathrm{rev}} \Lambda^{n_i^{\mathrm{rev}}}\Big]\!\Big] \theta_\kappa^{n_i^{\mathrm{rev}}} \Big]$$

where $\xi_{\alpha,i}$ denotes the stoichiometric coefficient corresponding to the αth species, and the appearing surface Damköhler numbers, $\mathrm{Da}_{\alpha,i}^{\mathrm{fwd}}$ and $\mathrm{Da}_{\alpha,i}^{\mathrm{rev}}$, are the ratios between the molar growth rate of the ALD film at the substrate and the speed of convective transport of the growth limiting species. Thus, $\mathrm{Da}_{\alpha,i}^{\mathrm{fwd}}$ and $\mathrm{Da}_{\alpha,i}^{\mathrm{rev}}$ are given by:

$$\mathrm{Da}_{\alpha,i}^{\mathrm{fwd}} := \Big[\!\Big[\frac{L}{\hat{v}_\zeta}\Big(\frac{A}{V}\Big) RT k_i^{\mathrm{fwd}} \Lambda^{n_i^{\mathrm{fwd}}}\Big]\!\Big] \tag{19}$$

$$\mathrm{Da}_{\alpha,i}^{\mathrm{rev}} := \Big[\!\Big[\frac{L}{\hat{v}_\zeta}\frac{M_\alpha}{\hat{\rho}\hat{\omega}_\alpha}\Big(\frac{A}{V}\Big) k_i^{\mathrm{rev}} \Lambda^{n_i^{\mathrm{rev}}}\Big]\!\Big] \tag{20}$$

3.4. Growth Surface State Dynamics

The characteristics of the surface reaction, in particular the probability that the reaction will proceed through the formation of adsorbed species, depends on the properties of the exposed adsorbent surface. The molar reaction rate per unit surface area (Eq. (16)) and the non-dimensional surface Damköhler numbers (Eqs. (19–20)) allow to determine the spatial and temporal fractional surface coverages:

$$\frac{\partial \theta_\kappa}{\partial \tau} = \Big[\!\Big[\frac{L}{\Lambda \hat{v}_\zeta}\Big]\!\Big] \sum_{i=1}^{N_i} \xi_{\kappa,i} r_i \tag{21}$$

$$:= \sum_{i=1}^{N_i} \xi_{\kappa,i} \Big[\!\Big[\frac{\hat{\rho}\hat{\omega}_\alpha}{M_\alpha}\Big(\frac{V}{A}\Big)\frac{1}{\Lambda}\Big]\!\Big] \Big[\mathrm{Da}_{\alpha,i}^{\mathrm{fwd}} \rho\omega_\alpha \Big(1 - \sum_{\forall \ell} \theta_\ell\Big)^{n_i^{\mathrm{fwd}}} - \mathrm{Da}_{\alpha,i}^{\mathrm{rev}} \theta_\kappa^{n_i^{\mathrm{rev}}}\Big]$$

$$0 = \sum_{\forall \kappa} \frac{\partial \theta_\kappa}{\partial \tau} \tag{22}$$

where θ_κ is the fractional surface coverage of the κth surface species, $\kappa \in \{A*, B*, C*\}$ (see Table 1). The non-dimensional term that appears in Eq.

(21) represents the precursor excess number and relates the maximum precursor molar density inside the reactor per unit adsorption site:

$$\gamma_\alpha := \left[\!\left[\frac{\hat{\rho}\hat{\omega}_\alpha}{M_\alpha}\left(\frac{V}{A}\right)\frac{1}{\Lambda}\right]\!\right] \tag{23}$$

3.5. Model Form and Size

The equations of the spatially distributed ALD reactor model that describe the gas-phase and growth surface state dynamics (see Sections 3.2–3.4), constitute a system of non-linear partial differential algebraic equations (PDAEs). In this study, the PDAE system was approximated using the method-of-lines (Davis, 1984; Schiesser, 1991) and the finite volume method (FVM). The first-order spatial derivative of the non-dimensional density, ρ, in Eq. (4) and of the gas-phase mass fractions, ω_α, in Eq. (6) have been approximated using a first-order downwind discretization scheme, while a first-order upwind discretization scheme was utilized to approximate the non-dimensional mass average velocity, v_ζ, in Eq. (5). The resulting non-linear index-1 differential-algebraic equation (DAE) system can be written collectively as:

$$\mathbf{0} = \mathbf{F}(\tau, \dot{\mathbf{x}}(\tau), \mathbf{x}(\tau), \mathbf{u}(\tau), \mathbf{w}(\tau), \boldsymbol{\beta}) \tag{24a}$$

$$\mathbf{0} = \mathbf{F}_0(\tau_0, \dot{\mathbf{x}}(\tau_0), \mathbf{x}(\tau_0), \mathbf{u}(\tau_0), \mathbf{w}(\tau_0), \boldsymbol{\beta}) \tag{24b}$$

$$\mathbf{0} = \mathbf{C_{eq}}(\tau_0, \tau_f, \mathbf{x}, \mathbf{u}, \mathbf{w}, \boldsymbol{\beta}) \tag{24c}$$

$$\mathbf{x}(\tau_0) = \mathbf{x}_0 \tag{24d}$$

where $\mathbf{F}$ is the DAE that represents the dynamics of the system, $\mathbf{F}_0$ represents the DAE augmented with additional initial conditions, $\mathbf{C_{eq}}$ is a point equality-constraint function (see Section 3.6), and $\boldsymbol{\beta}$ is the model parameter vector. Finally, $\mathbf{x} = [\rho, v_\zeta, \omega_\alpha, \theta_\kappa]^T$, $\mathbf{w} = [p, \theta_{C*}]^T$, and $\mathbf{u} = [\Delta\tau_\alpha, \dot{Q}_\alpha, T, \dot{V}_{\mathrm{VP}}]^T$ (where $\alpha \in \{A, B, C\}$ and $\kappa \in \{A*, B*\}$) describe dependent states, algebraic variables, and free design variables. Furthermore, with N_{FVM} FVM elements, the number of states, N_x, is $7N_{\mathrm{FVM}}$ and the number of algebraic variables, N_w, is $2N_{\mathrm{FVM}}$. The number of FVM elements is a compromise between accuracy and computational complexity, and should be chosen such that it gives adequate

representation of the dispersion. In this study, the number of FVM elements was set to 25.

3.6. Limit-cycle Criteria

For the purpose of this study, substrate effects on the nucleation and initial growth periods were not considered (see Section 2). For this reason, the solution strategy for the DAE system, $\mathbf{F}$, is to consider the limit-cycle dynamic solution that arises from the steady cyclic operation of the ALD reactor (Travis and Adomaitis, 2013a). Computation of limit-cycle solutions over the temporal horizon $[\tau_0, \tau_f]$ requires one additional important criterion: that the state variables, $\mathbf{x}$, return to their initial conditions at the end of the cycle, $\tau = \tau_f$:

$$\mathbf{x}(\tau_0) := \mathbf{x}(\tau_f) \tag{25a}$$

The following non-differentiated relationships must also be satisfied at $\tau \in \{\tau_0, \tau_f\}$, due to constraints that arise from the underlying assumptions on which Eqs. (4–6) and Eqs. (21–22) are based:

$$1 = \sum_{\forall \kappa} \theta_\kappa(\tau) \tag{25b}$$

$$1 = \sum_{\forall \alpha} \omega_\alpha(\tau) \tag{25c}$$

with $\kappa \in \{A*, B*, C*\}$, and $\alpha \in \{A, B, C, P\}$. Furthermore, the limit-cycle criteria in Eq. (25) are collected in the point equality-constraint function, $\mathbf{C_{eq}}$. Section 5 presents numerical aspects of computing limit-cycle solutions.

4. Scale-up Analysis

In order to maintain the dynamic similarity of gas flow and deposition when scaling up an ALD reactor, the Peclet, Reynold, surface Damköhler, and precursor excess numbers should be kept fixed. In this case, the flow path lines and non-dimensional distributions of concentrations will remain the same after the scale-up operation. The non-dimensional deposition rate and its relative uniformity will also remain the same. The overall objective of the scale up

analysis in the present study was to maintain a fixed absolute growth rate and its relative uniformity, while optimizing the precursor yield. Thus, the scale-up method can minimize individual precursor doses, while maintaining sufficiently high exposure levels, ensuring that the design specifications are not violated. The precursor yield can be expressed as:

$$\frac{dY_\alpha}{d\tau} = -\left[\!\!\left[\frac{A'\hat{\rho}\hat{v}_\zeta\hat{\omega}_\alpha}{\dot{Q}_\alpha\rho_{\mathrm{STP},\alpha}\Pi_\alpha(\tau,\Delta\tau_\alpha)}\right]\!\!\right](\rho v_\zeta\omega_\alpha)\big|_{\zeta=\zeta_{\mathrm{end}}} \tag{26}$$

subject to the initial value $Y_\alpha(\tau_0) = 1$. Moreover, the spatially dependent growth rate, m_{s}, in $\zeta \in [\zeta_0, \zeta_{\mathrm{end}}]$ is defined by:

$$\frac{\partial m_{\mathrm{s}}}{\partial \tau} = \sum_{i=1}^{N_i}\left[\!\!\left[\frac{\Lambda\Delta M_i}{\hat{m}_{\mathrm{s}}}\right]\!\!\right]\xi_{\kappa,i}\gamma_\alpha\left[\mathrm{Da}^{\mathrm{fwd}}_{\alpha,i}\rho\omega_\alpha\Big(1-\sum_{\forall\ell}\theta_\ell\Big)^{n_i^{\mathrm{fwd}}} - \mathrm{Da}^{\mathrm{rev}}_{\alpha,i}\theta_\kappa^{n_i^{\mathrm{rev}}}\right] \tag{27a}$$

subject to the initial value $m_{\mathrm{s}}(\tau_0) = 0$. Eq. (27a) uses the conversion rate of the fractional coverage of surface species (given by Eq. (21)). The scaling factor, $\hat{m}_{\mathrm{s}} = M_{\mathrm{s}}\Lambda$, corresponds to fully saturated ALD growth, and ΔM_i is the difference in molar mass of the outermost surface species that are governed by the ith elementary reaction (see Reaction (R2)). Eq. (27a) allows to determine the substrate spatially averaged growth rate:

$$\frac{d\langle m_{\mathrm{s}}\rangle}{d\tau} = \frac{1}{(\zeta_{\mathrm{end}}-\zeta_0)}\int_{\zeta_0}^{\zeta_{\mathrm{end}}}\frac{\partial m_{\mathrm{s}}}{\partial\tau}d\zeta \tag{27b}$$

In addition, by means of Eq. (27), the growth rate uniformity, UF, was conveniently defined as:

$$\mathrm{UF} = \begin{cases} 1 - \displaystyle\int_{\zeta_0}^{\zeta_{\mathrm{end}}}|m_{\mathrm{s}} - \langle m_{\mathrm{s}}\rangle|d\zeta\Big(\int_{\zeta_0}^{\zeta_{\mathrm{end}}} m_{\mathrm{s}}d\zeta\Big)^{-1} & \exists\zeta\in[\zeta_0,\zeta_{\mathrm{end}}]\ :\ m_{\mathrm{s}}(\zeta)>0 \\ 1 & \text{otherwise} \end{cases} \tag{28}$$

It is noteworthy that the uniformity metric defined in Eq. (28) describes the absolute deviation from the mean film mass accumulated, $\langle m_{\mathrm{s}}\rangle$, at normalized time τ. However, since the ALD process is an inherently forced periodic system, it is convenient to compare the performance of the existing design with that of the scaled-up design based on absolute normalized growth per cycle, $\langle m_{\mathrm{s}}\rangle(\tau_f)$,

where $\tau_f = (\hat{v}_\zeta/L)\Delta t$ is the end of the time horizon, $[\tau_0, \tau_f]$. The uniformity metric, $\mathrm{UF}(\tau_f)$, is evaluated in a similar manner at the end of the pulse sequence.

The duration of the αth precursor pulse, $\Delta\tau_\alpha$, is not explicitly taken into account by the non-dimensional parameters defined in Eqs. (7, 8 and 19–23), but it is can, instead, be conveniently expressed by the half-cycle average substrate exposure dose for the αth adsorptive precursor:

$$\frac{d\langle\delta_\alpha\rangle}{d\tau} = \left[\!\!\left[\frac{L}{\hat{v}_\zeta}\frac{\hat{\rho}\hat{\omega}_\alpha}{M_\alpha}RT\Delta\tau_\alpha\right]\!\!\right]\frac{1}{\Delta\tau_\alpha}\frac{1}{(\zeta_{\mathrm{end}}-\zeta_0)}\int_{\zeta_0}^{\zeta_{\mathrm{end}}}\rho\omega_\alpha d\zeta \tag{29}$$

subject to the initial value $\langle\delta_\alpha\rangle(\tau_0) = 0$. Moreover, the nominal αth exposure dose, ϕ_α, can be deduced from Eq. (29):

$$\phi_\alpha := \left[\!\!\left[\frac{L}{\hat{v}_\zeta}\frac{\hat{\rho}\hat{\omega}_\alpha}{M_\alpha}RT\Delta\tau_\alpha\right]\!\!\right] \tag{30}$$

However, to capture the increase in the total mass concentration during the precursor pulse, recall that $\hat{\rho}$ has been derived with $\Pi_\alpha := 0$ in Eq. (3), the nominal exposure dose, ϕ_α, must, therefore, be scaled accordingly:

$$\langle\hat{\delta}_\alpha\rangle = \frac{\phi_\alpha}{(1-\hat{\omega}_\alpha)} \tag{31}$$

The exposure dose of the growth surface to the αth precursor defined by Eq. (29) is characterized by the time dependent, local, partial pressure (Eq. (17)) during the exposure period, and during a portion of each purge period. The ALD gas–surface reactions must be coupled to the dynamic reactor transport model in order to model these features (see the systematic modeling approach described in Sections 3.2 and 3.4). Thus, there are two main ways of varying $\langle\delta_\alpha\rangle$: changing the mass flow of the precursors, $\dot{Q}_\alpha$, and in this way changing the partial pressure, or changing the duration of the pulse, $\Delta\tau_\alpha$. Eq. (29) thus adds a further dimension to the scale-up analysis, incorporating the effect of the dispersion of precursor pulses along the ζ-axis, and in this way enabling the precursor exposure dose to be accurately assessed in the scale-up analysis.

The set of process operating parameters that can be varied for the continuous cross-flow ALD reactor design with temporal precursor pulsing, in order

to maintain a fixed absolute growth rate, $\langle m_{\mathrm{s}} \rangle(\tau_f)$, and growth rate uniformity, $\mathrm{UF}(\tau_f)$, is $\mathbf{u} = [\Delta\tau_\alpha, \dot{Q}_\alpha, T, \dot{V}_{\mathrm{VP}}]^T$ and $\alpha \in \{A, B, P\}$. Table 2 lists the dimensional and non-dimensional parameters that are relevant to the scale-up methodology and the ways in which they depend on the set of manipulating variables, $\mathbf{u}$, and the length of the reactor.

4.1. Scale-up Methodology for Cross-flow ALD Reactor Designs

This paper analyses the implications of linearly scaling up an existing *Reactor* $\mathscr{A}$ (see Section 3) to a scaled-up *Reactor* $\mathscr{B}$ by a geometric factor $\lambda = L_{\mathscr{B}}/L_{\mathscr{A}}$. In particular, the various dimensional and non-dimensional parameters presented in Table 2 and the design criteria defined in Eqs. (27–29) are considered. The scale-up strategies presented here are based on a sequential methodology in which the way in which carrier gas manipulated variables, $[\dot{Q}_\beta, \dot{V}_{\mathrm{VP}}]$, depend on the dynamic similarity of gas flow is assessed first. The way in which the precursor pulse dose parameters, $[\dot{Q}_\alpha, \Delta\tau_\alpha]$ and $\forall\alpha \in \{A, B\}$, depend on the apparent ALD deposition rate and its relative uniformity is subsequently assessed.

4.1.1. Scaling Rules for the Process Operating Conditions

In the context of the carrier gas manipulated variables, two fundamentally different strategies (see also Table 2) were investigated when the reactor was scaled up, with $L \propto \lambda$:

i) *Scale-up strategy I* involves the reactor being scaled up without changing the carrier gas mass flow, $\dot{Q}_\beta$, or the flow rate through the vacuum pump, $\dot{V}_{\mathrm{VP}}$. The nominal pressure, $\hat{p}$, is unchanged when this strategy is used, while $\gamma_\alpha \mathrm{Da}_{\alpha,i}^{\mathrm{fwd}}$, $\langle \hat{\delta}_\alpha \rangle \propto \dot{Q}_\alpha \lambda^2$ for the αth precursor, and the residence time, $\hat{\tau} \propto \lambda^2$, change dramatically. The resulting increase in the product of the surface Damköhler number and precursor excess number, and the nominal precursor exposure dose with λ, are strictly positive, and give a higher efficiency of the deposition process in terms of precursor utilization and de-

Table 2: Scaling behavior of various dimensional and non-dimensional parameters. For the square duct that is being considered, the specific substrate surface area per unit reactor volume is $A/V = 2L^2/(L^2H)$ (m^{-1}) and the cross-sectional area is $A' = LH$ (m^2).

Variable	Dependence on L, $\dot{Q}_\beta$, $\dot{V}_{\mathrm{VP}}$, $\dot{Q}_\alpha$, $\Delta\tau_\alpha$	*Scale-up strategy I*: $L \propto \lambda$ $\dot{Q}_\beta = \text{const.}$ $\dot{V}_{\mathrm{VP}} = \text{const.}$	*Scale-up strategy II*: $L \propto \lambda$ $\dot{Q}_\beta \propto \lambda^\vartheta$ $\dot{V}_{\mathrm{VP}} \propto \lambda^\vartheta$
$\hat{v}_\zeta := \dfrac{\dot{V}_{\mathrm{VP}}}{A'}$	$\propto \dfrac{\dot{V}_{\mathrm{VP}}}{L}$	$\propto \lambda^{-1}$	$\propto \lambda^{\vartheta-1}$
$\hat{\rho} := \hat{p}\dfrac{M_\beta}{RT}$	$\propto \hat{p} \propto \dfrac{\dot{Q}_\beta}{\dot{V}_{\mathrm{VP}}}$	$-$	$-$
$\hat{\omega}_\alpha := \dfrac{\dot{Q}_\alpha\rho_{\mathrm{STP},\alpha}}{\dot{Q}_\alpha\rho_{\mathrm{STP},\alpha} + \dot{Q}_\beta\rho_{\mathrm{STP},\beta}}$	$\propto \dfrac{\dot{Q}_\alpha}{\dot{Q}_\beta}$ [a]	$\propto \dot{Q}_\alpha$	$\propto \dfrac{\dot{Q}_\alpha}{\lambda^\vartheta}$
$\hat{\tau} := \dfrac{L}{\hat{v}_\zeta}$	$\propto \dfrac{L^2}{\dot{V}_{\mathrm{VP}}}$	$\propto \lambda^2$	$\propto \lambda^{2-\vartheta}$
$\hat{\mu}$	$-$	$-$	$-$
$\hat{\mathscr{D}}_{\alpha\beta}$	$\propto \dfrac{1}{\hat{p}} \propto \dfrac{\dot{V}_{\mathrm{VP}}}{\dot{Q}_\beta}$	$-$	$-$
$\mathrm{Pe} := \dfrac{\hat{v}_\zeta L}{\hat{\mathscr{D}}_{\alpha\beta}}$	$\propto \dot{Q}_\beta$	$-$	$\propto \lambda^\vartheta$
$\mathrm{Re} := \dfrac{\hat{\rho}\hat{v}_\zeta L}{\hat{\mu}}$	$\propto \dot{Q}_\beta$	$-$	$\propto \lambda^\vartheta$
$\mathrm{Da}_{\alpha,i}^{\mathrm{fwd}} := \dfrac{L}{\hat{v}_\zeta}\Big(\dfrac{A}{V}\Big)RTk_i^{\mathrm{fwd}}\Lambda^{n_i^{\mathrm{fwd}}}$	$\propto \dfrac{L^2}{\dot{V}_{\mathrm{VP}}}$	$\propto \lambda^2$	$\propto \lambda^{2-\vartheta}$
$\mathrm{Da}_{\alpha,i}^{\mathrm{rev}} := \dfrac{L}{\hat{v}_\zeta}\dfrac{M_\alpha}{\hat{\rho}\hat{\omega}_\alpha}\Big(\dfrac{A}{V}\Big)k_i^{\mathrm{rev}}\Lambda^{n_i^{\mathrm{rev}}}$	$\propto \dfrac{L^2}{\dot{Q}_\alpha}$ [a]	$\propto \dfrac{\lambda^2}{\dot{Q}_\alpha}$	$\propto \dfrac{\lambda^2}{\dot{Q}_\alpha}$
$\gamma_\alpha := \dfrac{\hat{\rho}\hat{\omega}_\alpha}{M_\alpha}\Big(\dfrac{V}{A}\Big)\dfrac{1}{\Lambda}$	$\propto \dfrac{\dot{Q}_\alpha}{\dot{Q}_\beta}$ [a]	$\propto \dot{Q}_\alpha$	$\propto \dfrac{\dot{Q}_\alpha}{\lambda^\vartheta}$
$\gamma_\alpha\mathrm{Da}_{\alpha,i}^{\mathrm{fwd}} := \dfrac{L}{\hat{v}_\zeta}\dfrac{\hat{\rho}\hat{\omega}_\alpha}{M_\alpha}RTk_i^{\mathrm{fwd}}\Lambda^{n_i^{\mathrm{fwd}}-1}$	$\propto \dfrac{\dot{Q}_\alpha L^2}{\dot{Q}_\beta\dot{V}_{\mathrm{VP}}}$ [a]	$\propto \dot{Q}_\alpha\lambda^2$	$\propto \dot{Q}_\alpha\lambda^{2-2\vartheta}$
$\phi_\alpha := \dfrac{L}{\hat{v}_\zeta}\dfrac{\hat{\rho}\hat{\omega}_\alpha}{M_\alpha}RT\Delta\tau_\alpha$	$\propto \dfrac{\dot{Q}_\alpha\Delta\tau_\alpha L^2}{\dot{V}_{\mathrm{VP}}^2}$ [a]	$\propto \dot{Q}_\alpha\Delta\tau_\alpha\lambda^2$	$\propto \dot{Q}_\alpha\Delta\tau_\alpha\lambda^{2-2\vartheta}$
$\langle\hat{\delta}_\alpha\rangle := \dfrac{L}{\hat{v}_\zeta}\dfrac{\hat{\rho}}{M_\alpha}\dfrac{\hat{\omega}_\alpha}{\hat{\omega}_\beta}RT\Delta\tau_\alpha$	$\propto \dfrac{\dot{Q}_\alpha\Delta\tau_\alpha L^2}{\dot{V}_{\mathrm{VP}}^2}$	$\propto \dot{Q}_\alpha\Delta\tau_\alpha\lambda^2$	$\propto \dot{Q}_\alpha\Delta\tau_\alpha\lambda^{2-2\vartheta}$

[a] Only valid for $\dot{Q}_\alpha\rho_{\mathrm{STP},\alpha} \ll \dot{Q}_\beta\rho_{\mathrm{STP},\beta}$.

position rate. Finally, the Reynolds and Peclet numbers remain unchanged in this case, and thus dynamic similarity is preserved to some extent.

ii) *Scale-up strategy II* strives to maintain the reactor residence time, $\hat{\tau}$, and the nominal pressure, $\hat{p}$, constant by scaling the carrier gas flow rate and the flow rate through the vacuum pump in parallel, as $\dot{Q}_\beta$, $\dot{V}_{\mathrm{VP}} \propto \lambda^\vartheta$ with $\vartheta \in (0, 2]$. The residence time from the CSTR model is constant for $\vartheta := 2$, and *Scale-up strategy I* is obtained in the case in which $\vartheta := 0$. When this strategy is used, $\gamma_\alpha \mathrm{Da}_{\alpha,i}^{\mathrm{fwd}}$, $\langle \hat{\delta}_\alpha \rangle \propto \dot{Q}_\alpha \lambda^{2-2\vartheta}$ for the αth precursor and Re, Pe $\propto \lambda^\vartheta$. The way in which the product of the surface Damköhler number and the precursor excess number, and the nominal precursor exposure dose, change, makes it clear that the efficiency of the ALD process (in terms of precursor utilization and deposition rate) falls as ϑ increases.

It is beneficial when using *Scale-up strategy II* to use a low value of the residence time in cross-flow reactor designs, as this imposes a lower boundary onto the carrier gas purge time, $\Delta t_{\mathrm{P}} \propto \hat{\tau}$ (see, for example, Jur and Parsons (2011); Mousa et al. (2012)). This is needed in the ALD sequence to ensure negligible precursor interaction, and ultimately to maximize throughput in terms of the overall deposition rate per cycle time (see, for example, Holmqvist et al. (2013b)).

The deposition temperature, T, must be considered in a complete investigation of the carrier gas manipulated variables. Aarik et al. (2006) investigated experimentally the effects of deposition temperature, while Holmqvist et al. (2013b) and Travis and Adomaitis (2013b) carried out theoretical studies. The present investigation, however, is limited to $\mathbf{u} = [\dot{Q}_\beta, \dot{V}_{\mathrm{VP}}]$, since the temperature depends on growth per cycle in a convex manner (Puurunen, 2005), which means that its optimum value could be easily determined before the scale-up analysis. The optimal deposition temperature used in this study was determined from the study by Holmqvist et al. (2013b) and set to $T = 175$ (°C). The design specifications presented in Table 3 were determined in this way. The surface Damköhler number for desorption, $\mathrm{Da}_{\alpha,i}^{\mathrm{rev}}$ and $i = 3$, is not important at the optimum operating temperature (though included in the model), and it is only

relevant in the high temperature region where extensive dehydroxylation takes place (Deminsky et al., 2004; Matero et al., 2000; Rahtu et al., 2001) (see Eqs. (R2c–R2d)). Thus, the impact of the surface Damköhler number for desorption was not considered in the scale-up analysis.

4.1.2. Optimal Scaling Rules for the Precursor Exposure Dose

High uniformity is one of the key attributes of the ALD technology (Cleveland et al., 2012; Henn-Lecordier et al., 2011). Dynamic similarity is preserved to some extent when the scale-up strategies in Section 4.1.1 are applied. However, the growth rate, $\langle m_{\mathrm{s}} \rangle(\tau_f)$, and the uniformity of the deposition rate, $\mathrm{UF}(\tau_f)$, falls as ϑ increases unless the precursor exposure dose is properly scaled. This is, of course, not a desired result. Deposition rates and uniformities can be maintained by scaling the precursor pulse dose parameters, $\mathbf{u} = [\dot{Q}_\alpha, \Delta\tau_\alpha]$ and $\forall \alpha \in \{A, B\}$. The scaling rules deduced from Table 2 demonstrate how the free design variables depend on the metrics relevant in the scale-up strategies in a mechanistic manner, even though they are based solely on the CSTR model (see Section 3.1). The half-cycle average substrate exposure dose for the αth precursor (Eq. (29)), in particular, introduces a complex interdependency between the mass flow, $\dot{Q}_\alpha$, the pulse duration, $\Delta\tau_\alpha$, and the resulting local partial pressure dynamics throughout the spatial domain, $\zeta \in [\zeta_0, \zeta_{\mathrm{end}}]$. Furthermore, the uniformity of the film thickness (Eq. (27)) is inherently spatially dependent, and thus cannot be reproduced by the CSTR model.

For these reasons, an optimization problem was formulated in order to distinguish the proper scaling factors of $\mathbf{u} = [\dot{Q}_A, \dot{Q}_B]$. The present investigation was limited to the optimization of the precursor mass flows, since Holmqvist et al. (2013b) have recently shown that the optimal precursor pulse durations, $\Delta\tau_\alpha$ and $\forall \alpha \in \{A, B\}$, are always at the lower boundary of the assigned range when precursor utilization and overall deposition rate per cycle time are targeted. Therefore, the precursor pulse duration in the scaled up *Reactor* $\mathscr{B}$ was set to that of *Reactor* $\mathscr{A}$ (see Table 3). Thus, in order to penalize high values

of the decision variables, $\mathbf{u}$, the cost function was defined as:

$$\Phi(\mathbf{y},\mathbf{u}) = -\sum_{\alpha\in\{A,B\}}\int_{\tau_0}^{\tau_f}\frac{dY_\alpha}{d\tau}d\tau \tag{32}$$

and assembles the precursor yields (Eq. (26)). The cost function was optimized while fulfilling the requirements placed on deposition rate and its uniformity by incorporating the terminal inequality constraints:

$$\mathrm{C_{ieq}}^{\langle m_\mathrm{s}\rangle} = \langle m_\mathrm{s}\rangle^{\mathscr{A}}(\tau_f) - \langle m_\mathrm{s}\rangle^{\mathscr{B}}(\tau_f) \tag{33a}$$

$$\mathrm{C_{ieq}}^{\mathrm{UF}} = \mathrm{UF}^{\mathscr{A}}(\tau_f) - \mathrm{UF}^{\mathscr{B}}(\tau_f) \tag{33b}$$

which can be collectively written as $\mathbf{C_{ieq}} = [\mathrm{C_{ieq}}^{\langle m_\mathrm{s}\rangle}, \mathrm{C_{ieq}}^{\mathrm{UF}}]^T$. Table 3 lists the optimal design variables and resulting design criteria for *Reactor* $\mathscr{A}$ used in Eq. (33). Finally, the dynamic optimization problem (DOP) in the time interval $\tau \in [\tau_0, \tau_f]$ of achieving the assigned design criteria (see Eqs. (27b–29)) in the scaled-up design *Reactor* $\mathscr{B}$ may be stated using the cost function, Φ, as:

$$\min_{\mathbf{u},\,\mathbf{x}_0}\ \Phi(\mathbf{y},\mathbf{u}) \tag{34}$$

$$\begin{aligned}
\text{s.t.}\quad & \mathbf{0} = \mathbf{F}(\tau,\dot{\mathbf{x}},\mathbf{x},\mathbf{w},\mathbf{u},\boldsymbol{\beta})\\
& \mathbf{0} = \mathbf{F}_0(\tau_0,\dot{\mathbf{x}}(\tau_0),\mathbf{x}(\tau_0),\mathbf{u}(\tau_0),\mathbf{w}(\tau_0),\boldsymbol{\beta})\\
& \mathbf{y} = \mathbf{g_y}(\mathbf{x},\mathbf{w},\mathbf{u},\boldsymbol{\beta})\\
& \mathbf{0} \geq \mathbf{C_{ieq}}(\tau_0,\tau_f,\mathbf{x},\mathbf{u},\mathbf{w},\boldsymbol{\beta})\\
& \mathbf{0} = \mathbf{C_{eq}}(\tau_0,\tau_f,\mathbf{x},\mathbf{u},\mathbf{w},\boldsymbol{\beta})\\
& \mathbf{x}_{\min} \leq \mathbf{x} \leq \mathbf{x}_{\max},\quad \mathbf{w}_{\min} \leq \mathbf{w} \leq \mathbf{w}_{\max}\\
& \mathbf{u}_{\min} \leq \mathbf{u} \leq \mathbf{u}_{\max},\quad \mathbf{x}(\tau_0) = \mathbf{x}_0
\end{aligned}$$

where $\mathbf{g_y}$ is the response function (Eqs. (26–28)) that governs the model output, and where $\mathbf{y} = [\langle m_\mathrm{s}\rangle, \mathrm{UF}, Y_\alpha]^T$, with $\alpha \in \{A, B\}$, is used to define the cost function and terminal inequality constraints of the DOP. An important implication of this formulation of the simultaneous optimization problem is that it enables the limit-cycle criteria (see Section 3.6) to be satisfied while maximizing the precursor yields (Eq. (26)). Thus, the initial values, $\mathbf{x}_0$, are set to be free

Table 3: *Reactor* $\mathscr{A}$ design specifications used in terminal inequality constraints, $\mathbf{C_{ieq}} = [{C_{ieq}}^{\langle m_s \rangle}, {C_{ieq}}^{UF}]^T$, and those that must be satisfied in the scaled-up *Reactor* $\mathscr{B}$ for each geometric factor, λ.

Design variables			Design criteria		
T	$1.75 \cdot 10^2$	(°C)	$\langle m_s \rangle^{\mathscr{A}}(\tau_f)^a$	$9.00 \cdot 10^{-1}$	(cycle^{-1})
$\dot{Q}_\alpha$	$1.83 \cdot 10^1$	(sccm)	$Y_A^{\mathscr{A}}(\tau_f)^b$	$3.59 \cdot 10^{-2}$	(cycle^{-1})
$\dot{Q}_\beta$	$5.00 \cdot 10^2$	(sccm)	$Y_B^{\mathscr{A}}(\tau_f)^b$	$3.53 \cdot 10^{-2}$	(cycle^{-1})
$\hat{\tau}\Delta\tau_\alpha$	$2.00 \cdot 10^{-2}$	(s)	$\text{UF}^{\mathscr{A}}(\tau_f)^a$	$9.50 \cdot 10^{-1}$	(cycle^{-1})
$\hat{\tau}\Delta\tau_\beta$	1.00	(s)	$\langle \delta_A \rangle^{\mathscr{A}}(\tau_f)^b$	2.68	(Pa s)
$p\|_{\zeta=\zeta_{end}}$	$3.00 \cdot 10^2$	(Pa)	$\langle \delta_B \rangle^{\mathscr{A}}(\tau_f)^b$	2.68	(Pa s)
$\dot{V}_{VP}{}^c$	$4.62 \cdot 10^{-3}$	($\text{m}^3\,\text{s}^{-1}$)			

[a] Assigned reference value in Eq. (33).
[b] Determined with optimized design variables from Eq. (34).
[c] Determined from Eq. (3c) and $\mathbf{u} = [T, \dot{Q}_\beta, p|_{\zeta=\zeta_{end}}]^T$.

when solving Eq. (34), and varied such that the equality constraint relations are satisfied at $\tau \in \{\tau_0, \tau_f\}$ (Eq. (25)).

5. Modeling and Optimization Environment

Modelica (The Modelica Association, 2012) was used as the description language for the dynamic ALD process model developed in this paper. Modelica is an equation-based language for complex physical models, whose underlying mathematical formalism is that of DAEs. The open-source platform JModelica.org (Åkesson et al., 2010) was used for simulation and optimization of the Modelica model. In the context of simulation, JModelica.org was used to compile the Modelica model into a functional mock-up unit (FMU) (Blochwitz et al., 2011), thus transforming it from a DAE form into an ordinary differential equation (ODE) form. JModelica.org's interface to SUNDIALS (Hindmarsh et al., 2005) was subsequently used to simulate the model. The user interacts with the various components of JModelica.org using the Python scripting language.

5.1. Dynamic Optimization of DAEs Using Direct Collocation with CasADi

To enable the formulation of the DOP (see Eq. (34)) based on the model (see Eq. (24)) described by Modelica code, the Modelica extension Optimica (Åkesson, 2008) has been developed and integrated into JModelica.org. The algorithm used in the work described in this paper to solve the DOP uses a direct and local collocation method (Biegler, 2010) on finite elements, using Radau points and Lagrange interpolation polynomials (Magnusson and Åkesson, 2012). The algorithm has been implemented in Python in the JModelica.org framework, using the computer algebra system with automatic differentiation (CasADi) optimization package (Andersson et al., 2012). Using CasADi's symbolic syntax, it is possible to transcribe the DOP into a finite dimensional non-linear programming problem (NLP). The NLP was subsequently solved using the primal-dual interior point method IPOPT v.3.10.3 (Wächter and Biegler, 2006), using MA27 as a linear solver. The first and second derivatives required by IPOPT are automatically and efficiently generated by CasADi, using automatic differentiation (AD) techniques.

The time horizon of the DOP in Eq. (34) was set to $\tau \in [0, 2.8] \cdot \hat{\tau}^{-1}$ (a.u.), corresponding to a single pulse sequence (see Table 3), and the collocation scheme used had 50 finite elements with three Radau points in each. The state and algebraic variables were approximated using Lagrange polynomials of order three and two, respectively. As all trajectories over the time horizon are solved for simultaneously when using a collocation method, good initial guesses of the state and algebraic variables at the collocation points are crucial. For this reason, the result of a simulation from the initial stationary point (through imposing stationarity on Eq. (24) under non-reactive conditions (Section 3.1)) was used as the initial guess.

6. Results and Discussion

This paper describes two inherently different scale-up strategies, outlined in Section 4.1.1. It is, however, vital for both strategies that the CSTR model

(Section 3.1) is valid, as it governs the scaling behavior of the non-dimensional parameters in Table 2. The validity of the CSTR model can be assessed by determining the discrepancy between $\hat{\tau} = L/\hat{v}_\zeta$ and the apparent spatially averaged reactor chamber residence time, defined as:

$$\langle \hat{\tau} \rangle := \left[\!\!\left[\frac{L}{\hat{v}_\zeta} \right]\!\!\right] (\zeta_{\text{end}} - \zeta_0) \left(\int_{\zeta_0}^{\zeta_{\text{end}}} v_\zeta d\zeta \right)^{-1} \tag{35}$$

where v_ζ is governed by the compressible Navier–Stokes equation (Eq. (5)). In order for the relationship $\langle \hat{\tau} \rangle := \hat{\tau}$ to be valid, the spatially averaged normalized velocity field described by Eq. (5) must be equal to one. Thus, analyzing the Navier–Stokes equation shows that this relationship is valid only if the shear stress, Φ_ζ, approaches zero. A small discrepancy between $\hat{\tau}$ and $\langle \hat{\tau} \rangle$, however, is expected for low values of Φ_ζ. The validity of the CSTR model has been assessed when calculating the results for both scale-up strategies.

6.1. Scale-up Strategy I

Fig. 1 shows the cost function entities, $Y_\alpha(\tau_f)$ and $\alpha \in \{A, B\}$, and the terminal inequality constraint entities, $\langle m_\text{s} \rangle(\tau_f)$ and $\text{UF}(\tau_f)$, as functions of the geometric factor, λ, when applying *Scale-up strategy I*. The results have been determined for the optimal precursor mass flows, $\dot{Q}_A^{\mathscr{B}} := \dot{Q}_B^{\mathscr{B}}$. Thus, the mass flows of the two precursors were set to be equal and determined from solving the DOP (Eq. (34)) for each $\lambda \in [1, 20]$. The assigned design specifications for *Reactor* $\mathscr{A}$, listed in Table 3, have been retained with $\lambda = 1$, and the quotient between the metrics associated with *Reactor* $\mathscr{B}$ and those associated with *Reactor* $\mathscr{A}$ are denoted by the superscript $\mathscr{B}/\mathscr{A}$. As expected from the quadratic scaling behavior of $\hat{\tau}$ with λ in Table 2, the relative apparent reactor residence time, $\langle \hat{\tau} \rangle^{\mathscr{B}/\mathscr{A}}$, depends in a linear manner on λ on a logarithmic scale with base two. By this means, the validity of the CSTR model is valid in these conditions. In contrast, the optimal relative precursor mass flows, $\dot{Q}_\alpha^{\mathscr{B}/\mathscr{A}}$, depend on λ in a weakly exponential manner, in order for the inequality constraints to be fulfilled to the specified tolerances. In addition, the relative

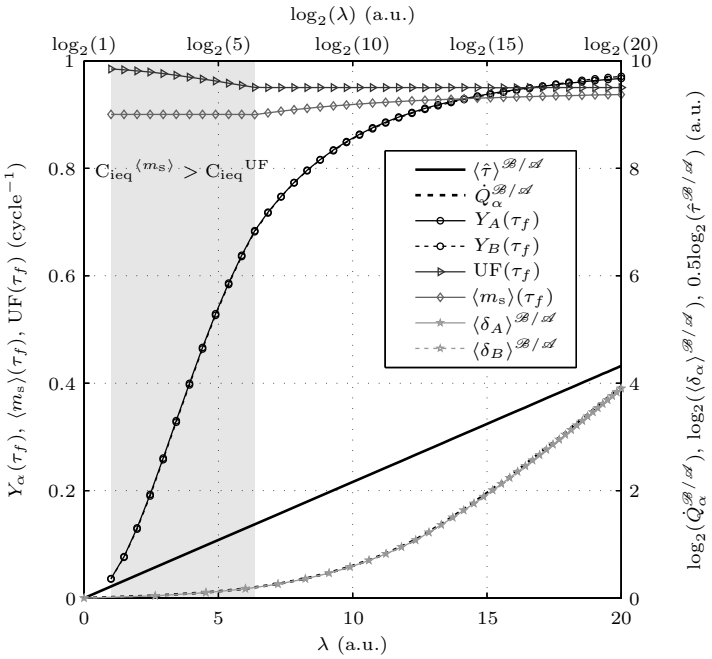

Figure 1: The effects of the geometrical factor, $\lambda \in [1, 20]$, and the optimal precursor mass flow, $\dot{Q}_\alpha$ and $\alpha \in \{A, B\}$, (which were set to be equal) on the cost function entities and the terminal inequality constraints when applying *Scale-up strategy I*. The shaded area represents the geometric scaling factors for which the terminal inequality constraint for $\langle m_\mathrm{s} \rangle(\tau_f)$ is active.

apparent precursor exposure doses, $\langle \delta_\alpha \rangle^{\mathscr{B}/\mathscr{A}}(\tau_f)$ and $\alpha \in \{A, B\}$, determined from Eq. (29) with all gas–surface reactions switched off (i.e. $S_\alpha := 0$ and $\alpha \in \{A, B, C\}$), depend on λ in a similar manner as the optimal relative precursor mass flows.

More importantly, Fig. 1 shows that two different regimes appear, depending on the value of the geometric factor, λ, since only one of the terminal inequality constraints, $\mathbf{C_{ieq}} = [\mathrm{C_{ieq}}^{\langle m_\mathrm{s} \rangle}, \mathrm{C_{ieq}}^{\mathrm{UF}}]^T$, is active for each λ. The terminal inequality constraint for $\mathrm{UF}(\tau_f)$ is active for $\lambda \leq 6.5$ when the reference values of *Reactor* $\mathscr{A}$ given in Table 3 are used, whereas the constraint for $\mathrm{UF}(\tau_f)$ is active for $\lambda > 6.5$. This implies that the film thickness uniformity constraint is more easily satisfied than the deposition rate per cycle at lower substrate di-

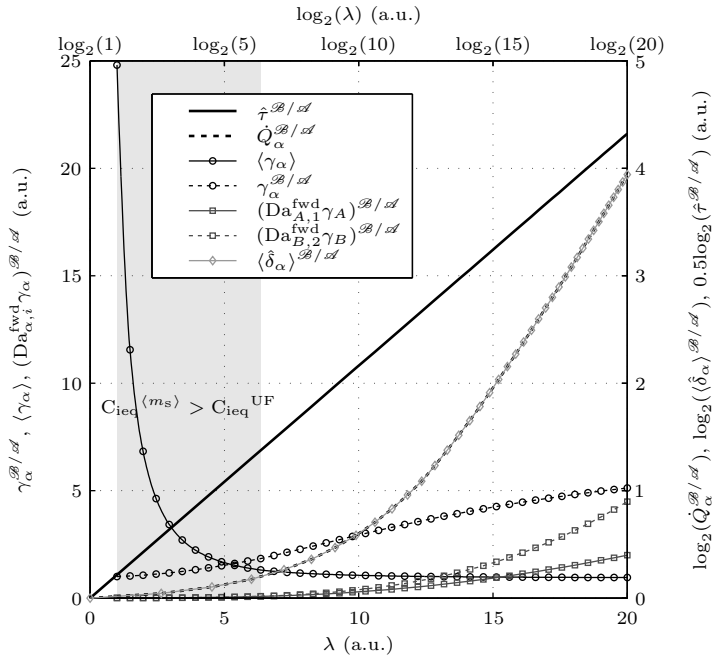

Figure 2: The effects of the geometrical factor, $\lambda \in [1, 20]$, and the optimal precursor mass flow, $\dot{Q}_\alpha$ and $\alpha \in \{A, B\}$, (which were set to be equal) on the non-dimensional parameters listed in Table 2 when applying *Scale-up strategy I*. The shaded area represents the geometric scaling factors for which the terminal inequality constraint for $\langle m_\mathrm{s} \rangle(\tau_f)$ is active.

mensions, when optimizing precursor yields. Moreover, the extent of the region in which ${\mathrm{C_{ieq}}}^{\langle m_\mathrm{s} \rangle} > {\mathrm{C_{ieq}}}^{\mathrm{UF}}$ is smaller at higher values of the assigned reference $\langle m_\mathrm{s} \rangle^{\mathscr{A}}(\tau_f)$ of *Reactor* $\mathscr{A}$. The maximum growth rate per cycle, in particular, is obtained for $\langle m_\mathrm{s} \rangle^{\mathscr{A}}(\tau_f) := 1$, at which value the film thickness uniformity is equal to one. Finally, Fig. 1 also shows that the optimal precursor yield approaches unity as $\lambda \to 20$. This implies that the precursor utilization increases with scale up when applying *Scale-up strategy I*.

One of the conditions imposed by *Scale-up strategy I* is that the reactor is scaled up without changing any of the operating parameters, $\dot{Q}_\beta$ and $\dot{V}_{\mathrm{VP}}$. Further, dynamic similarity will be maintained to some extent as Re and Pe remain unchanged, whereas the remaining dimensionless numbers in Table 2 will

change. Fig. 2 shows these dimensionless numbers as functions of $\lambda \in [1, 20]$. The way in which the relative reactor chamber residence time, $\hat{\tau}^{\mathscr{B}/\mathscr{A}}$, and the relative apparent precursor exposure doses, $\langle \hat{\delta}_\alpha \rangle^{\mathscr{B}/\mathscr{A}}(\tau_f)$ and $\alpha \in \{A, B\}$ (Eq. (30)), depend on the geometrical factor resemble those of their apparent counterparts shown in Fig. 1. The product of the relative surface Damköhler number and the precursor excess number, $(\mathrm{Da}^{\mathrm{fwd}}_{\alpha,1}\gamma_\alpha)^{\mathscr{B}/\mathscr{A}}$ and $\alpha \in \{A, B\}$, increases strictly with λ when the optimal precursor mass flows are used. This metric is essential since it is a major factor in determining the fractional surface coverage (Eq. (21)), and the resulting deposition rate (Eq. (27a)). Thus, the increase in $\mathrm{Da}^{\mathrm{fwd}}_{\alpha,1}\gamma_\alpha$ with λ and $\dot{Q}_\alpha$ causes the inherent benefits in precursor utilization when the substrate dimension is scaled up, as shown in Fig. 1. The excess number, γ_α, however, (as defined in Eq. (23)) is only valid for a specific time instant, and thus cannot describe the entire molar amount of precursors injected during a single pulse. The total molar amount of precursors injected per molar unit adsorption site, $\langle \gamma_\alpha \rangle$, was defined for this reason as:

$$\langle \gamma_\alpha \rangle := \frac{\dot{Q}_\alpha \rho_{\mathrm{STP},\alpha} \hat{\tau} \Delta\tau_\alpha}{\Lambda A M_\alpha} \tag{36}$$

Fig. 2 shows that $\langle \gamma_\alpha \rangle$ decreases strictly with λ when the optimal precursor mass flows are used. Moreover, approximately 25 times the saturation molar amount is required for the terminal inequality constraints to be satisfied at $\lambda = 1$, in these conditions. In contrast, the value of $\langle \gamma_\alpha \rangle$ asymptotically approaches unity as $\lambda \to 20$, and ultimately promotes the increase in precursor utilization. Finally, Eq. (36) allows to calculate the maximum theoretical precursor yield from the inverse of $\langle \gamma_\alpha \rangle$, i.e. $\max Y_\alpha(\tau_f) := \langle \gamma_\alpha \rangle^{-1}$.

6.1.1. Film Thickness Uniformity

Fig. 3 shows the true implication of optimizing the precursor yields in scale-up studies. It is evident that optimizing the cost function of precursor utilization, subject to the inequality constraint of film thickness uniformity, creates a strong coverage gradient towards the trailing edge of the substrate as $\lambda \to 20$. This is a consequence of the cross-flow ALD reactor design, which means that

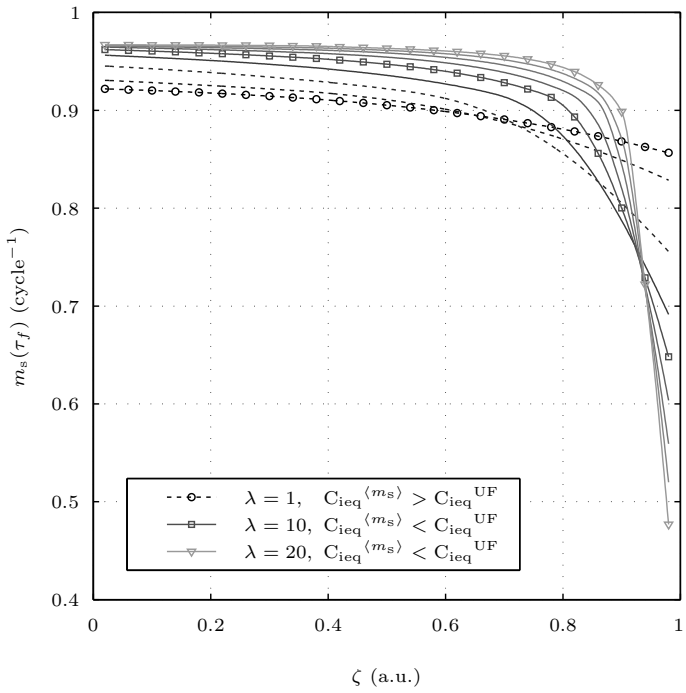

Figure 3: Film thickness profiles as functions of the non-dimensionalized spatial coordinate variable, $\zeta \in [0, 1]$, sampled for $\lambda \in [1, 20]$ when applying *Scale-up strategy I*. (- -) indicates the geometric scaling factors for conditions in which the terminal inequality constraint for $\langle m_s \rangle(\tau_f)$ is active.

the trailing edge of the substrate is exposed to a more depleted precursor flow than the leading edge, and that the cross-substrate film deposition rate is always inhomogeneous to some extent. Accordingly, the optimal precursor yields approach unity for high values of the geometric factor (see Fig. 1), and only a very small amount of the injected precursor dose is available for reaction close to the trailing edge. This causes the deposition rate to approach zero rapidly in this region. In contrast, the gradients in this region are significantly gentler for low values of λ, such as those associated with low precursor yields and values of $\langle \gamma_\alpha \rangle \gg 1$. It is, however, noteworthy that the terminal inequality constraint for deposition rate uniformity is satisfied for all the profiles shown in Fig. 3. Recall that the uniformity metric that was defined in Eq. (28) relates the absolute

deviation of the deposition rate to its spatially averaged mean value. In order to enforce gentler gradients of $m_{\mathrm{s}}(\tau_f)$ towards the trailing edge of the substrate, it is suggested that $\mathrm{UF}(\tau_f)$ can be redefined to describe simply the relative accumulated mass, $m_{\mathrm{s}}|_{\zeta=\zeta_{\mathrm{end}}}$, at $\zeta = \zeta_{\mathrm{end}}$, since the deposition rate will always be a minimum here in the cross-flow reactor design. This formulation overcomes the limitation of a spatially averaged metric (Eq. (28)), while still providing the physical interpretation of a perfectly uniform profile for $\mathrm{UF}(\tau_f) := 1$.

6.1.2. Gas-phase Limit-cycle Dynamics

Fig. 4 shows the limit-cycle solution for the gas-phase state and algebraic variables when using *Scale-up strategy I* and a geometric factor of $\lambda = 20$. It is evident that the state and algebraic variables conform to periodic boundary conditions over the time horizon $[\tau_0, \tau_f]$. The markers indicate the locations of the Radau collocation points for $\zeta \in \{1/2, N_{\mathrm{FVM}} - 1/2\} \cdot (\zeta_{\mathrm{end}} - \zeta_0)/N_{\mathrm{FVM}}$ (i.e. the centers of the first and last FVM elements). The CSTR model dynamic reactor gas-phase material balances (Eq. (1)) have been extended to incorporate the instantaneous formulation of the surface-state dynamics (Eq. (21)) and the accumulated mass deposited (Eq. (27a)), in order to make it possible to compare the results from the complete CSTR model with those obtained from the spatially distributed PDAE model (Eq. (24)). Dashed lines in Fig. 4 show the results from the extended CSTR model.

Fig. 4a shows that the nominal velocity, $\hat{v}_\zeta$, (Eq. (3d)) is prescribed at $\zeta = \zeta_{\mathrm{end}}$ through Eq. (14). The output from the CSTR model follows that of the distributed PDAE model (Eq. (24)) at the outlet, as expected, but it should be remembered that the center of the last FVM element is located at $\zeta = (N_{\mathrm{FVM}} - 1/2) \cdot (\zeta_{\mathrm{end}} - \zeta_0)/N_{\mathrm{FVM}}$. The pressure effects propagate instantaneously throughout the spatial domain, $\zeta \in [\zeta_0, \zeta_{\mathrm{end}}]$, during the precursor exposure periods (which are indicated by shaded rectangles) (Fig. 4c), whereas the density of the gas mixture propagates with the mass average velocity (Fig. 4b). During the subsequent purge period, the chamber pressure drops in the manner of a first-order dynamical system with a single time constant given by

the ratio of chamber volume to pumping speed (Travis and Adomaitis, 2013a,b). The base-line pressure, $\hat{p}$ (Eq. (3c)), is approached during the subsequent purge for $\zeta = (N_{\mathrm{FVM}} - 1/2) \cdot (\zeta_{\mathrm{end}} - \zeta_0)/N_{\mathrm{FVM}}$, but it is not fully attained in the conditions studied here.

More importantly, the spatial distributions of v_ζ and ρ (Figs. 4a and 4b) result from the pressure drop across the reactor chamber (Fig. 4c). This pressure drop is ultimately governed by the compressible formulation of the continuity equation and the Navier–Stokes equation (Eqs. (4–5)), and it is determined by the chamber dimensions and process operating parameters $[\dot{V}_{\mathrm{VP}}, \dot{Q}_\beta, T]$. The resulting pressure drop across the reactor chamber that originates from the non-zero shear stress, Φ_ζ, in Eq. (5) implies that the cross-substrate film thickness deposition rate (Eq. (27a)) is always inhomogeneous despite the injected precursor exposure dose, $\langle \delta_\alpha \rangle$. Consequently, it is a combination of the degree of precursor depletion in the flow direction and the magnitude of the pressure drop across the reactor chamber that governs the extent of the deposition profile non-uniformity (see Fig. 3). Moreover, it is noteworthy that Eq. (10) governs that the pressure drop across the reactor chamber is higher for low-volume reactor designs with high aspect ratios, $L/H \gg 1$, and for high carrier gas linear velocities.

Finally, the results from the distributed PDAE model (Eq. (24)) in Fig. 4d shows that the αth precursors are separated at all positions of the spatial domain, $\zeta \in [\zeta_0, \zeta_{\mathrm{end}}]$. Especially, the high precursor utilization at this geometric factor ensures that negligible amounts of precursor remain after each exposure period in the gas phase, at the start of the subsequent precursor exposure dose period. Undesirable CVD conditions are in this way avoided, as recently investigated by Travis and Adomaitis (2013a). However, Fig. 1 shows that the number of reactor chamber volumes purged during the carrier gas purge period, $(\hat{\tau}\Delta\tau_\beta)/\langle\hat{\tau}\rangle$ (cf. Eq. (35)), decreases linearly with the apparent residence time from that of the base-case *Reactor* $\mathscr{A}$ when applying *Scale-up strategy I*. Thus, when the large precursor doses that are associated with lower yields are used, excess precursors remain in the gas phase and the carrier gas purge may be

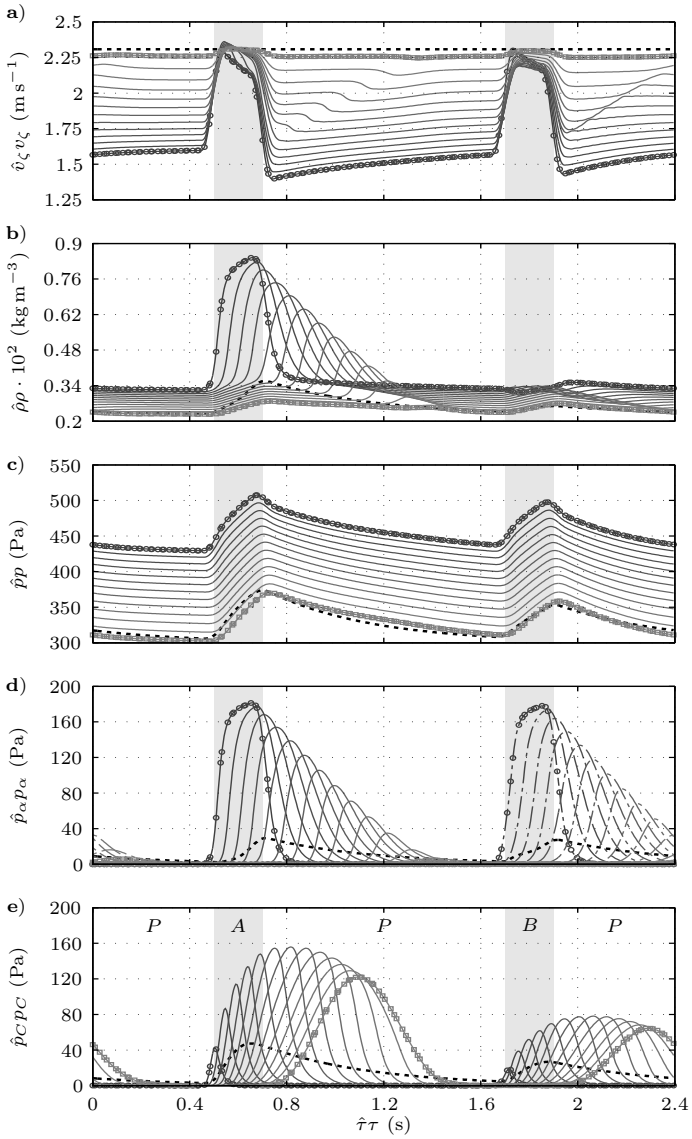

Figure 4: Scaled-up *Reactor* $\mathscr{B}$ gas-phase dynamics for a single-pulse horizon $\tau \in [\tau_0, \tau_f]$ and $\lambda = 20$ when using *Scale-up strategy I*. The limit-cycle solution is spatially resolved for $\zeta = (\jmath - 1/2)(\zeta_{\text{end}} - \zeta_0)/N_{\text{FVM}}$ and $\jmath \in \{1, 3, \cdots, N_{\text{FVM}}\}$. $(- \circ -)$ indicates the state and algebraic variables for $\jmath = 1$, while $(-\square-)$ indicates the corresponding variables for $\jmath = N_{\text{FVM}}$. (--) indicates the limit-cycle solution from the CSTR model. The shaded areas indicate the precursor pulse interval endpoints.

insufficient. It is expected that this phenomenon will be more pronounced at shorter purge periods. In addition, the limit-cycle solution obtained from the CSTR model depicted in Fig. 4d shows that non-negligible amounts of precursors remain in the gas phase from the previous precursor exposure at the start of the subsequent precursor exposure for the given residence time. This will become more evident when examining the accumulated mass trajectory in Section 6.1.3.

6.1.3. Growth Surface Limit-cycle Dynamics

Fig. 5 shows the limit-cycle solutions for the growth surface state and algebraic variables obtained using *Scale-up strategy I* and a geometric factor of $\lambda = 20$. The spatially distributed mass gain trajectory (Fig. 5a) determined from Eq. (27) can be physically interpreted by means of the underlying chemical composition of the growth surface (Figs. 5b–5d). In particular, the net contribution from the irreversible reactions (R2a–R2b) to Eq. (27b) is the degree of saturation of the fractional surface coverage onto which the respective precursors can adsorb, and the difference in molar masses, ΔM_i (where $i \in \{1, 2, \cdots, 4\}$), of the adsorptive precursors and the associated number of ligands that desorb from the growth surface. Thus, the difference in molecular mass between the initial and terminal surface species in Reaction (R2a), $\Delta M_1 = M_{\mathrm{Zn(C_2H_5)_2}} - \nu M_{\mathrm{C_2H_6}}$, results in a net mass increase, whereas that of Reaction (R2b), $\Delta M_2 = M_{\mathrm{H_2O}} - (2 - \nu) M_{\mathrm{C_2H_6}}$, results in the net contribution to Eq. (27) from this half-reaction being less than zero, when $\nu = 1.37$. The significant difference in net mass contribution to Eq. (27) from each precursor half-reaction is reflected also in the trajectory of the deposition rate uniformity (Fig. 5a). This trajectory falls at the start of the $\mathrm{Zn(C_2H_5)_2}$ precursor period and passes through a minimum, as the travelling wave of the precursor propagates across the substrate. The uniformity subsequently rises when the entire substrate has been exposed. The corresponding effect of the subsequent $\mathrm{H_2O}$ precursor exposure is not as pronounced, which is a consequence of the small difference in molecular mass between the initial and terminal surface species in

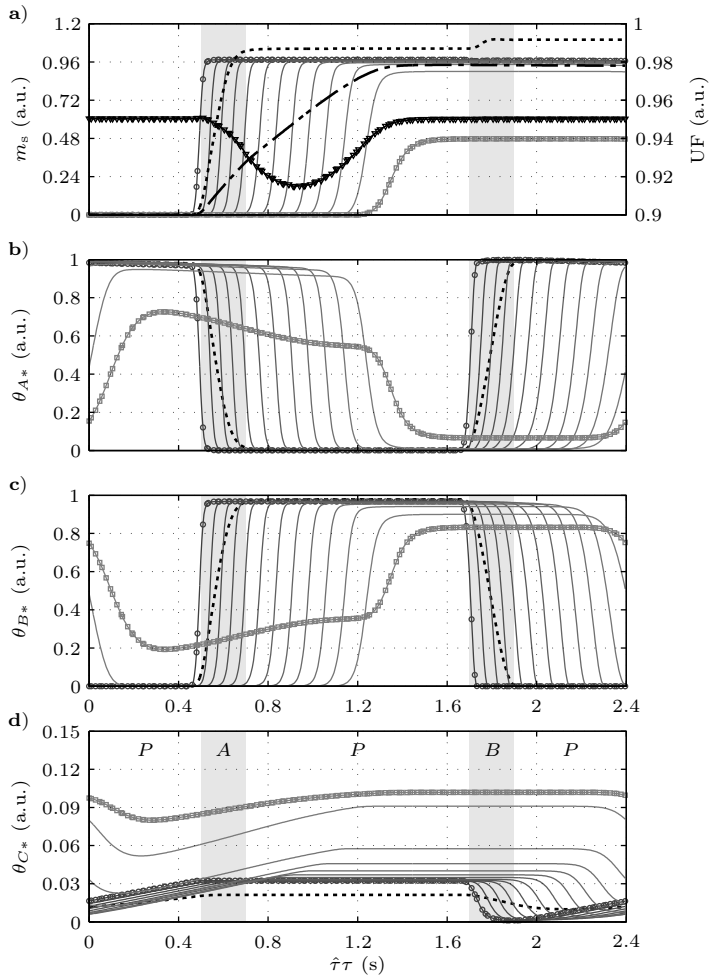

Figure 5: Scaled-up *Reactor* $\mathscr{B}$ film-growth dynamics for a single-pulse horizon $\tau \in [\tau_0, \tau_f]$ and $\lambda = 20$ when applying *Scale-up strategy I*. The limit-cycle solution is spatially resolved for $\zeta = (\jmath - 1/2)(\zeta_{\text{end}} - \zeta_0)/N_{\text{FVM}}$ and $\jmath \in \{1, 3, \cdots, N_{\text{FVM}}\}$. $(- \circ -)$ indicates the state and algebraic variables for $\jmath = 1$, while $(-\square-)$ indicates the corresponding variables for $\jmath = N_{\text{FVM}}$. (--) indicates the limit-cycle solution from the CSTR model, while $(- \cdot -)$ indicates the substrate spatially averaged deposition rate, and $(-\triangledown-)$ the uniformity of the film thickness. The shaded areas indicate the precursor pulse interval endpoints.

Reaction (R2b). It is also evident from Fig. 5a that the terminal inequality constraints for $\langle m_{\text{s}} \rangle(\tau_f)$ and $\text{UF}(\tau_f)$ are satisfied.

As the travelling wave of the $Zn(C_2H_5)_2$ precursor propagates through the

reactor, the partial pressure, p_A, becomes lower in the direction of the flow (Fig. 4d). As discussed in Section 6.1.1 and 6.1.2, this phenomenon originates from the pressure drop (cf. Eq. (10)) across the reactor chamber and the conversion of available surface OH ligands through Reaction (R2a). As this reaction continues, the coverage of $\theta_{A*} \to 0$ as the growth surface saturates with $B*$. The subsequent H_2O precursor exposure and half-reaction (see Reaction (R2b)) proceed in an analogous manner, ultimately resulting in the reformation of $A*$. The degree of saturation at each position in $[\zeta_0, \zeta_{\text{end}}]$ is governed by the partial pressure of precursors in the vicinity of the growth surface (see Eq. (16)). Thus, as $p_\alpha \to 0$ in the region close to the trailing edge of the substrate, the conversion rate of surface species falls significantly as the reaction rate $r_i \to 0$. This causes the sharp decrease in deposition rate shown in Fig. 5a and in Fig. 3. Likewise, the trailing edge of the substrate is also subject to the most severe dehydroxylation (see Fig. 5d), due to the low H_2O precursor dose level in this region, which limits the rate of Reaction (R2d). The dehydroxylation reaction continues throughout the purge period following H_2O exposure, which reduces the ligand density of surface OH groups, and ultimately the overall deposition rate.

Fig. 5a shows that there is a clear distinction between the accumulated mass trajectory, $\langle m_{\text{s}} \rangle$, determined from the spatially distributed PDAE model (Eq. (24)) and that determined from the CSTR model. As expected, the CSTR model predicts an instantaneous net mass increase at the start of each precursor exposure period, whereas the PDAE model predicts a net mass increase that is related to the propagation of the travelling wave of precursors throughout the spatial domain. In addition, the mass gain trajectory from the CSTR model clearly shows the implication of the coexistence of precursors in the gas phase, as previously described in Section 6.1.2. Recall that the maximum growth rate per cycle is obtained for $\langle m_{\text{s}} \rangle(\tau_f) := 1$, and a net mass decrease is expected from the H_2O half-reaction (Reaction (R2b)). A net mass increase in $\langle m_{\text{s}} \rangle$ is, however, predicted by the CSTR model during the H_2O precursor exposure, and its terminal value exceeds one (which means that more than a single mono-

layer is deposited). However, the model does not describe the gas-phase CVD reactions, instead this phenomenon arises from the adsorption of the remaining $Zn(C_2H_5)_2$ precursor in the gas-phase onto the newly formed OH ligands on the growth surface, which are, in turn, converted instantaneously throughout Reaction (R2b). In contrast, the PDAE model does not predict undesirable CVD conditions, and the accumulated mass trajectory that the model predicts agrees with that expected to arise in true ALD conditions.

6.2. Scale-up Strategy II

Fig. 6 shows the cost function entities, $Y_\alpha(\tau_f)$ and $\alpha \in \{A, B\}$, and the terminal inequality constraint entities, $\langle m_s \rangle(\tau_f)$ and $\mathrm{UF}(\tau_f)$, as functions of the geometric factor, λ, sampled for $\vartheta \in (0, 2]$ when using *Scale-up strategy II*. The results have been calculated with the minimum precursor mass flows, $\dot{Q}_A^{\mathscr{B}} := \dot{Q}_B^{\mathscr{B}}$, that satisfy the terminal inequality constraints (Eq. (33)) for each value of λ and ϑ. In order to maintain the nominal mass fraction for the αth precursor (Eq. (3b)) in the scaled-up *Reactor* $\mathscr{B}$, it is necessary that $d\log_2(\dot{Q}_\alpha^{\mathscr{B}/\mathscr{A}})/(d\log_2(\lambda)) := \vartheta$ (see also Table 2). However, there is a clear discrepancy between the optimal precursor mass flows, $\dot{Q}_\alpha^{\mathscr{B}/\mathscr{A}}$, and $\dot{Q}_\alpha^{\mathscr{B}/\mathscr{A}} := \lambda^\vartheta$ for all $\vartheta \in [0, 2]$ shown in Fig. 6d. For this reason, the scaling rule for the nominal mass fraction, i.e. $\dot{Q}_\alpha^{\mathscr{B}/\mathscr{A}} := \lambda^\vartheta$, is considered not adequate to achieve the assigned design criteria in the scaled-up design *Reactor* $\mathscr{B}$.

Fig. 6c shows that the highest precursor yields, $Y_\alpha(\tau_f)$, are obtained when scaled-up *Reactor* $\mathscr{B}$ is operated at the lowest possible carrier gas mass flow, $\dot{Q}_\beta$. As was the case for *Scale-up strategy I*, precursor utilization increases strictly with λ when using *Scale-up strategy II*. However, for $\vartheta = 2$ (which corresponds to maintaining constant reactor residence time, $\hat{\tau}$, as indicated in Table 2) approximately the same yield is obtained for all $\lambda \in \{1, 20\}$. This is a consequence of the way in which the product of the surface Damköhler number and precursor excess number, $\gamma_\alpha \mathrm{Da}_{\alpha,i}^{\mathrm{fwd}} \propto \dot{Q}_\alpha \lambda^{2-2\vartheta}$ for the αth precursor, depends on ϑ. Thus for $\vartheta = 2$, the inherent increase in this non-dimensional metric, ultimately promotes the reaction rate through Eq. (21) and the resulting deposition rate

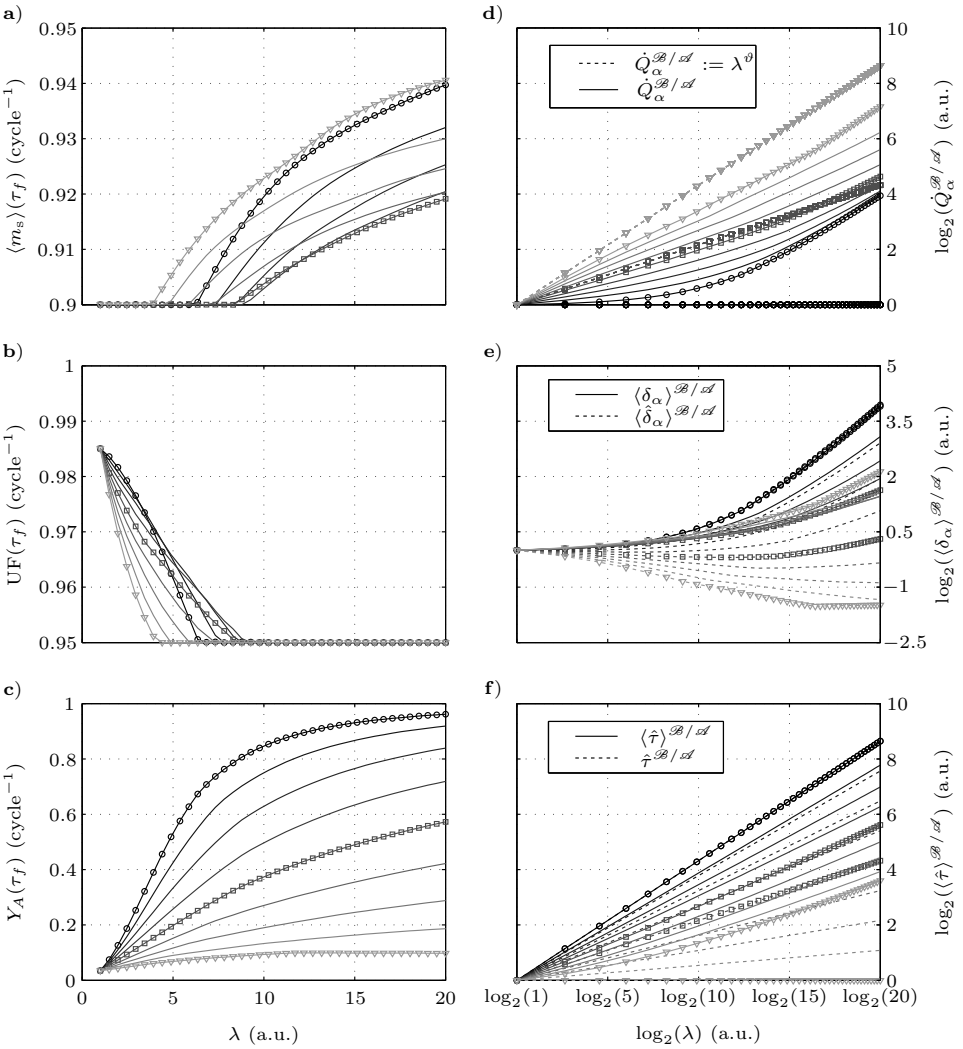

Figure 6: The effects of the geometrical factor, $\lambda \in [1, 20]$, the optimal precursor mass flow, $\dot{Q}_\alpha$ and $\alpha \in \{A, B\}$, (which are set to be equal) on the cost function entities and terminal inequality constraint entities when using *Scale-up strategy II*, with $\vartheta \in (0, 2]$. ($\circ$) indicates the solution for $\vartheta = 0.0$ (i.e. that of *Scale-up strategy I*), while ($\square$) indicates that for $\vartheta = 1.0$, and ($\triangledown$) that for $\vartheta = 2.0$.

through Eq. (27), with the geometric scaling factor is lost.

More importantly, Figs. 6e and 6f show clearly that the discrepancies between the apparent reactor residence time, $\langle \hat{\tau} \rangle$, and the apparent precursor

exposure dose, $\langle\delta_\alpha\rangle$, from their respective non-dimensional counterparts, $\hat{\tau}$ and $\langle\hat{\delta}_\alpha\rangle$, increases as $\vartheta \to 2$. These discrepancies arise from the pressure drop across the spatial domain, $\zeta \in [\zeta_0, \zeta_{\text{end}}]$, (see Section 6.1.2 and Fig. 4c) and result in the spatial distribution of v_ζ and ρ. For this reason, a higher averaged linear flow rate, $\langle v_\zeta\rangle$ is necessary to maintain a constant residence time, $\hat{\tau}$, as $\lambda \to 20$. Thus, larger pressure drops are obtained as $\lambda \to 20$ and as the linear flow rate increases, since $\Phi_\zeta \propto v_\zeta$ in Eq. (10), subject to $\dot{Q}_\beta$, $\dot{V}_{\text{VP}} \propto \lambda^\vartheta$. This gives the larger discrepancies shown in Figs. 6e and 6f under these conditions. In particular, $\hat{\tau}$ is maintained for the scaled-up *Reactor* $\mathscr{B}$ proposed in Table 2, whereas its apparent value, $\langle\hat{\tau}\rangle$, increases strictly with the geometric factor. In contrast, these values, and those of the precursor exposure dose, coincide over the entire range of $\lambda \in [0, 20]$ when using *Scale-up strategy I*. In conclusion, the non-dimensional variables in Table 2 and the CSTR model become less valid as $\vartheta \to 2$. Thus, the results reported here clearly motivate the utility of the spatially distributed PDAE model in combination with dynamic optimization methods for maximizing the precursor utilization in the scaled-up system while maintaining fixed absolute growth rate and its relative uniformity.

Fig. 6a shows that $\langle m_{\text{s}}\rangle(\tau_f)$ depends on ϑ in a weakly convex manner for each value of $\lambda \in [10, 20]$. Fig. 7 shows this more clearly, where $\langle m_{\text{s}}\rangle(\tau_f)$ is plotted as a function of ϑ and sampled for $\lambda \in [10, 20]$. The terminal inequality constraint for the deposition rate uniformity is active at these geometric factors. Figs. 7a and 7c show the noteworthy result that the highest values of both $\langle m_{\text{s}}\rangle(\tau_f)$ and $Y_A(\tau_f)$ are obtained for $\lambda = 20$ in the entire range, $\vartheta \in (0, 2]$. The magnitude of the normalized deposition rate per cycle is governed to a large extent by the apparent precursor exposure dose, $\langle\delta_\alpha\rangle$. Thus, it can be concluded that the weak convex dependence of relative apparent exposure dose with ϑ, shown in Fig. 7b underlies the dependence of $\langle m_{\text{s}}\rangle(\tau_f)$ shown in Fig. 7a. The magnitude of the apparent precursor exposure dose (Eq. (30)), in turn, arises from the spatially distributed pressure across the reactor and the mass fraction of the injected precursor pulse, $\hat{\omega}_\alpha$. In this context, larger pressure drops are obtained as $\vartheta \to 2$ and as the linear flow rate increases, since $\Phi_\zeta \propto v_\zeta$,

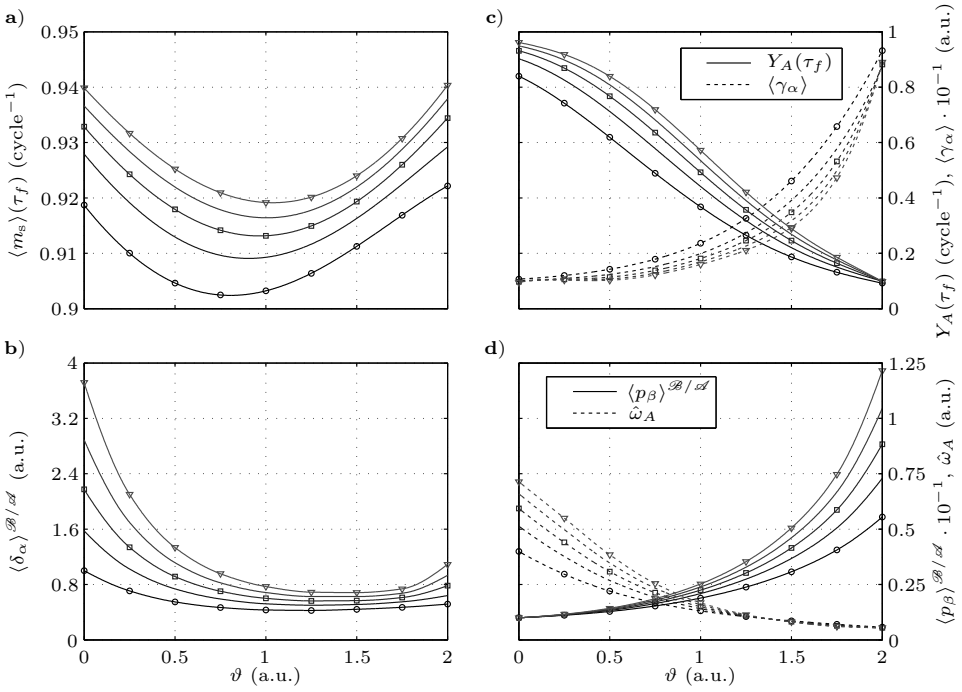

Figure 7: The effects of the geometrical factor, $\lambda \in \{10, 12.5, 15, 17.5, 20\}$, and the optimal precursor mass flow, $\dot{Q}_\alpha$ and $\alpha \in \{A, B\}$, (which were set to be equal) on the cost function entities and terminal inequality constraints when using *Scale-up strategy II* with $\vartheta \in (0, 2]$. ($\circ$) indicates the solution for $\lambda = 10$, ($\square$) for $\lambda = 15$, and ($\triangledown$) for $\lambda = 20$.

subject to $\dot{Q}_\beta$, $\dot{V}_{\mathrm{VP}} \propto \lambda^\vartheta$. This is clearly shown in Fig. 7d, where the spatially averaged stationary carrier gas pressure, $\langle p_\beta \rangle$, is plotted as a function of ϑ. In addition, the precursor mass fraction decreases with ϑ, as a consequence of the minimal precursor mass flows, which must ensure that the terminal inequality constraints (see Eq. (33)) are satisfied, and the assigned carrier gas mass flow, $\dot{Q}_\beta \propto \lambda^\vartheta$, determined from the scaling rules in Table 2 (Fig. 7d). Therefore, the compromise between the steeper pressure gradient and the lower precursor mass fractions causes the observed convex dependence of $\langle \delta_\alpha \rangle$ on $\vartheta \in [0, 2]$.

Moreover, Fig. 7b makes it clear that significantly higher molar amounts of precursors must be injected per molar unit adsorption site, $\langle \gamma_\alpha \rangle$, as $\vartheta \to 2$, and the precursor yield falls accordingly. Thus, the film thickness profiles shown in

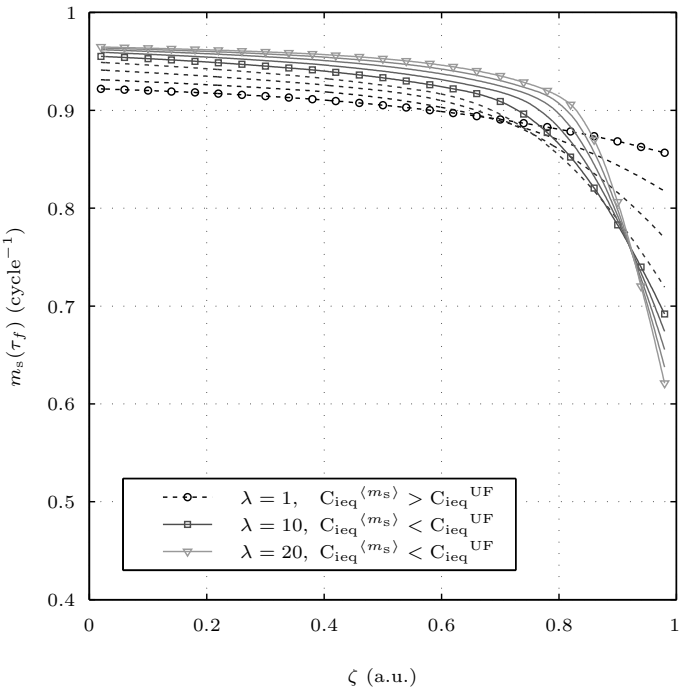

Figure 8: Film thickness profiles as functions of the non-dimensionalized spatial coordinate variable, $\zeta \in [0, 1]$, sampled for $\lambda \in [1, 20]$ when using *Scale-up strategy II* with $\vartheta = 0.5$. (--) indicates the geometric scaling factors for those profiles for which the terminal inequality constraint for $\langle m_s \rangle(\tau_f)$ is active.

Fig. 8 for $\vartheta = 0.5$ are more uniform for higher geometric factors than those obtained when using *Scale-up strategy I* (Fig. 3), since the overall precursor yields are lower when *Scale-up strategy II* is used. It is, however, important to remember that the negative pressure gradient in the ζ-direction (Fig. 4c) also influences the deposition rate through the precursor partial pressure: it lowers the driving force for the reaction closer to the trailing edge of the substrate, and thereby contributes to the formation of a non-uniform deposition profile.

6.2.1. Gas-phase and Growth Surface Limit-cycle Dynamics

The reason for exploring *Scale-up strategy II* was to develop a method which provides a sufficient length of the purge period to remove precursors in the gas

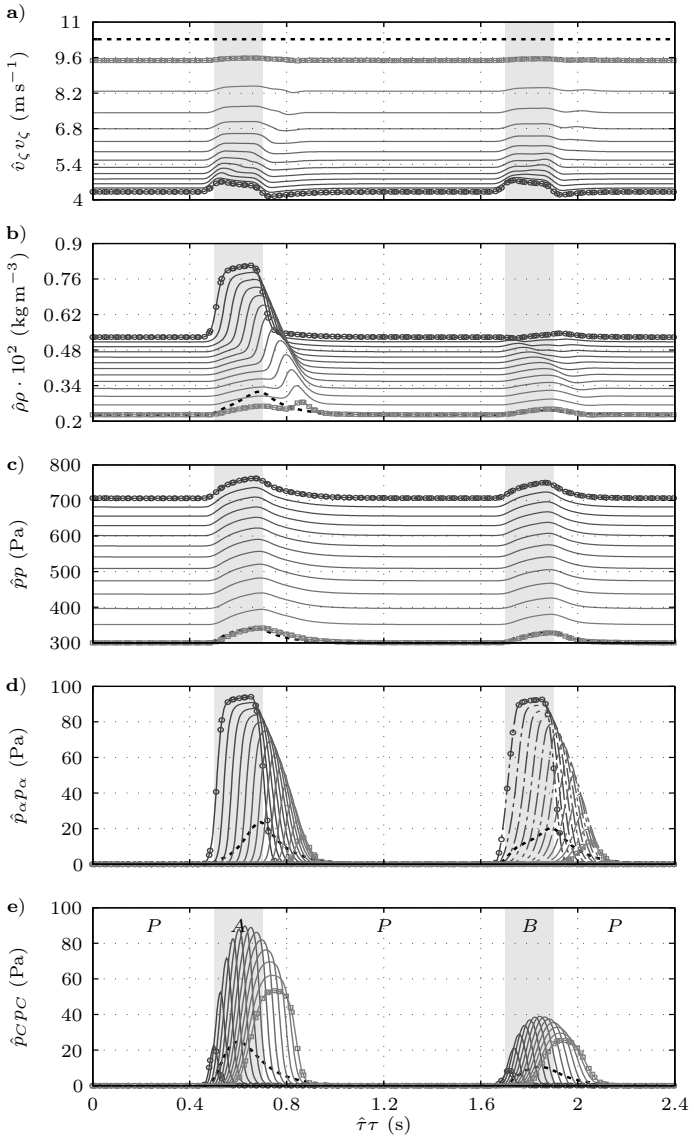

Figure 9: Scaled-up *Reactor* $\mathscr{B}$ gas-phase dynamics for a single-pulse horizon $\tau \in [\tau_0, \tau_f]$ and $\lambda = 20$ when using *Scale-up strategy II* with $\vartheta = 0.5$. The limit-cycle solution is spatially resolved for $\zeta = (\jmath - 1/2)(\zeta_{\text{end}} - \zeta_0)/N_{\text{FVM}}$ and $\jmath \in \{1, 3, \cdots, N_{\text{FVM}}\}$. $(- \circ -)$ indicates the state and algebraic variables for $\jmath = 1$, while $(-\square-)$ indicates the corresponding variables for $\jmath = N_{\text{FVM}}$. (--) indicates the limit-cycle solution from the CSTR model. The shaded areas indicate the precursor pulse interval endpoints.

phase remaining from the previous exposure period at the start of the subsequent precursor period. This was achieved by reducing the reactor chamber residence time while maintaining the nominal carrier gas pressure, $\hat{p}$. Fig. 9 shows the limit-cycle solution for the gas-phase state and algebraic variables when using *Scale-up strategy II*, a geometric factor $\lambda = 20$, and $\vartheta = 0.5$. The results show clearly the implications of the scaling rule for the carrier gas manipulated variables, i.e. $\dot{Q}_\beta$, $\dot{V}_{\mathrm{VP}} \propto \lambda^\vartheta$, from Table 2. The travelling wave of precursors and the density of the gas mixture propagate with a significantly higher mass average velocity as expected. In addition, the overall higher mass average velocity gives rise to a significantly higher negative pressure gradient in the ζ-direction than that shown in Fig. 4. Moreover, at the start of the purge period, the total pressure relaxes to the stationary value of the carrier gas partial pressure at each position in the spatial domain, $\zeta \in [\zeta_0, \zeta_{\mathrm{end}}]$. In particular, the total pressure at $\zeta = (N_{\mathrm{FVM}} - 1/2) \cdot (\zeta_{\mathrm{end}} - \zeta_0)/N_{\mathrm{FVM}}$ relaxes to the base-line pressure, $\hat{p}$, and this trajectory resembles that of the CSTR model.

More importantly, it is evident that the reduction in residence time, which arises as a consequence of prescribing $\dot{Q}_\beta$, $\dot{V}_{\mathrm{VP}} \propto \lambda^\vartheta$ with $\vartheta = 0.5$, is sufficient to ensure that the gas-phase precursors and the reaction by-products are transported out of the reactor chamber (at all positions) before the start of the subsequent precursor pulse period. In addition, the stationary carrier gas partial pressure is maintained after a fraction of the purge period, when assigned to $\hat{\tau}\Delta\tau_P := 1.0$ (s). Likewise, the appearance of the accumulated mass trajectory during the precursor exposures (see Fig. 10) shows that precursors do not coexist in the gas phase. These results confirm that the carrier gas pulse period can be reduced for this set of $\dot{Q}_\beta$, $\dot{V}_{\mathrm{VP}} \propto \lambda^\vartheta$ and $\vartheta = 0.5$. The growth rate per cycle time, $\hat{\tau}\Delta\tau$, can in this way be significantly reduced, as previously shown in Holmqvist et al. (2013b). Alternatively, the reactor chamber residence time can be safely increased, while preventing the undesirable CVD conditions, by choosing $\vartheta < 0.5$. In any case, there is no reason to choose $\vartheta > 0.5$, since this causes a reduction in the precursor mass fractions and the partial pressures (Fig. 9d), and lowers the overall precursor yield (Figs. 6 and 7).

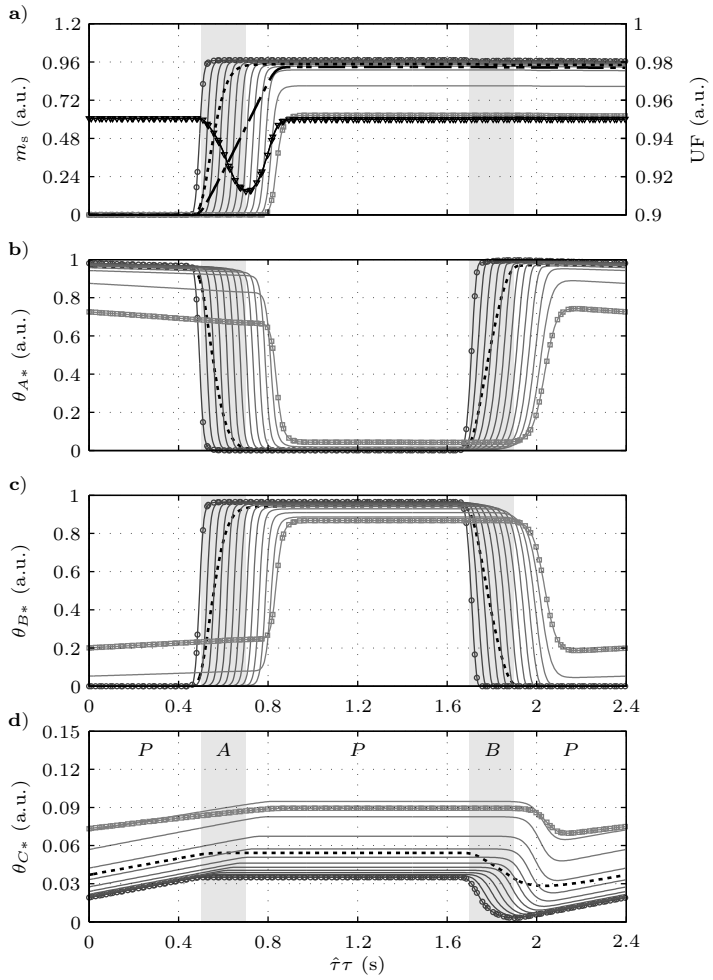

Figure 10: Scaled-up *Reactor* $\mathscr{B}$ film-growth dynamics for a single-pulse horizon $\tau \in [\tau_0, \tau_f]$ and $\lambda = 20$ when using *Scale-up strategy II* with $\vartheta = 0.5$. The limit-cycle solution is spatially resolved for $\zeta = (\jmath - 1/2)(\zeta_{\text{end}} - \zeta_0)/N_{\text{FVM}}$ and $\jmath \in \{1, 3, \cdots, N_{\text{FVM}}\}$. $(- \circ -)$ indicates the state and algebraic variables for $\jmath = 1$, while $(-\square-)$ indicates the corresponding variables for $\jmath = N_{\text{FVM}}$. (- -) indicates the limit-cycle solution from the CSTR model, while $(-\cdot-)$ indicates the substrate spatially averaged deposition rate and $(-\triangledown-)$ its film thickness uniformity. The shaded areas indicate the precursor pulse interval endpoints.

7. Concluding Remarks

This paper presents a novel model-based methodology for scaling up continuous cross-flow ALD reactor systems that use temporally separated precursor

pulsing. The overall objective of the scale-up method was to maintain dynamic similarity associated with identical absolute growth rates and to maintain uniformity close to that of the base-case reactor, while maximizing precursor utilization. A one-dimensional, physically-based process model was developed that integrates components that describe the reactor-scale gas-phase dynamics and surface-state dynamics with experimentally validated surface reaction kinetics from previous studies (Holmqvist et al., 2012, 2013a). By this means, dynamic similarity was investigated by constructing all equations that governs the gas-phase and surface-state algebraic variables, together with their boundary and initial conditions, in non-dimensional form. The impact of the geometric scaling factor and the process manipulated variables on the non-dimensional variables was subsequently thoroughly investigated.

The scale-up method developed comprises two steps: the carrier gas manipulated variables are scaled in parallel to maintain various degrees of dynamic similarity in the scaled-up reactor, and the mass flow of precursors is subsequently optimized to give maximum yields under the terminal constraints of absolute deposition rate and its relative uniformity. To describe accurately the steady cyclic operation of the ALD reactor, the limit-cycle dynamic solution that arises in this way was discretized using a collocation scheme in time. The optimization problem is fully discretized in the collocation method by approximating state algebraic and control variables by Lagrange polynomials, which results in one large NLP. This NLP is solved simultaneously for all state, algebraic and control variables that describe the approximated trajectories and this ensures that the limit-cycle criteria, and the terminal design criteria, are fulfilled.

In particular, it was demonstrated that the maximum precursor yields were promoted at higher substrate dimensions. Consequently, the trailing edge of the substrate was exposed to a lower precursor dose, and caused in this way strong deposition rate gradients in this region. Moreover, the results showed that higher carrier gas linear velocities gave rise to larger pressure drops across the reactor chamber, and thereby contributed significantly to the formation of a

non-uniform deposition profile. In conclusion, it is a combination of the degree of precursor depletion in the flow direction and the magnitude of the pressure drop across the reactor chamber that governs the extent of the deposition profile non-uniformity. In addition, the interaction between dose and purge periods was revealed by analyzing the spatially distributed limit-cycle dynamic solution for the gas-phase precursor partial pressures, and the solution obtained for the resulting accumulated mass gain trajectory. By this means, process regimes were identified in which surface reactions occurred under CVD conditions. True ALD conditions, associated with fully decoupled binary precursor doses, could be retained by lowering the reactor chamber residence time at the expense of lower precursor utilization.

The proposed scaling rules are based on nominal algebraic and state variables determined from the CSTR model. The validity of the CSTR model has been assessed by examining the discrepancy between the nominal and the apparent reactor chamber residence times, and between precursor exposure doses. Results shown here indicate that these discrepancies are higher for low-volume reactor designs with high aspect ratios, $L/H \gg 1$, and for high carrier gas linear velocities. The CSTR model, however, is valid over a wider range of geometrical scaling factors for reactor designs with lower aspect ratios. The results reported here clearly motivate the utility of models based on PDAEs in combination with dynamic optimization methods for maximizing the precursor utilization in the scaled-up system while maintaining a high value of the growth rate per cycle, which ensures acceptable reactor throughput. The result is a short set of optimal scaling guidelines that can be followed to maintain deposition profiles and chemistry identical when adapting a laboratory-scale thin-film process to meter-scale manufacturing equipment. These guidelines allow the knowledge obtained and methods developed when working with centimeter-scale substrates to be directly and easily translated to larger reactors.

Acknowledgement

This work has been supported by the Swedish Research Council under Grant no. 2006-3738. Fredrik Magnusson is a member of the LCCC Linnaeus Center and the eLLIIT Excellence Center at Lund University.

Nomenclature

Roman letters

A	substrate surface area	m^2
A'	cross section area of the reaction chamber	m^2
$\mathbf{C_{eq}}$, $\mathbf{C_{ieq}}$	equality and inequality constraint vector	–
$\mathrm{Da}_{\alpha,i}$	surface Damköhler number	–
$\hat{\mathscr{D}}_{\alpha\beta}$, $\mathscr{D}_{\alpha\beta}$	binary diffusivity	$\mathrm{m}^2\,\mathrm{s}^{-1}$, –
$\mathbf{F}$	system of differential algebraic equations	–
$\mathbf{g}$	response function	–
H	reactor height	m
k_i	reaction rate constant	$(\mathrm{mol\,m}^{-2})^{1-n_i}\,\mathrm{Pa}^{-1}\,\mathrm{s}^{-1}$, $(\mathrm{mol\,m}^{-2})^{1-n_i}\,\mathrm{s}^{-1}$
L	reactor chamber length	m
M_α	molar mass	$\mathrm{kg\,mol}^{-1}$
$\hat{m}_\mathrm{s}$, m_s	film mass increment	$\mathrm{kg\,m}^{-2}$, –
n_i	surface reaction order	–
Pe	Peclet number	–
$\hat{p}$, p	pressure	Pa, –
$\dot{Q}_\alpha$	volumetric flow rate at STP	$\mathrm{Nm}^3\mathrm{s}^{-1}$
R	universal gas constant	$\mathrm{J\,mol}^{-1}\,\mathrm{K}^{-1}$
Re	Reynolds number	–
r_i	surface reaction rate	$\mathrm{mol\,m}^{-2}\,\mathrm{s}^{-1}$
S_α	source term in the general transport equation	$\mathrm{kg\,m}^{-3}\,\mathrm{s}^{-1}$
T	temperature	K
t	dimensional time	s
UF	film thickness uniformity factor	–
$\mathbf{u}$	design variables	–
V	reactor chamber volume	m^3
$\dot{V}_\mathrm{VP}$	volumetric flow rate of the vacuum pump	$\mathrm{m}^3\,\mathrm{s}^{-1}$
$\hat{v}_\zeta$, v_ζ	linear velocity	$\mathrm{m\,s}^{-1}$, –
$\mathbf{w}$	algebraic variables	–
$\mathbf{x}$	state variables	–
Y_α	precursor yield	cycle^{-1}

$\mathbf{y}$	model output variables	–
z	dimensional spatial coordinate	m

Greek letters

$\boldsymbol{\beta}$	model parameter vector	–
γ_α	excess number	–
Δt_α, $\Delta\tau_\alpha$	pulse duration	s, –
$\hat{\delta}_\alpha$, δ_α	half-cycle average precursor dose	Langmuir
ζ	non-dimensional spatial coordinate	–
θ_κ	fractional surface coverage of surface species	–
Λ	maximum molar concentration of surface sites	$\mathrm{mol\,m^{-2}}$
λ	geometric scaling factor	–
$\hat{\mu}$, μ	dynamic viscosity of the gas mixture	$\mathrm{kg\,m^{-1}\,s^{-1}}$, –
ν	numbers of surface OH groups reacting	
	with each $Zn(C_2H_5)_2$	–
ξ_i	surface reaction stoichiometric coefficient	–
$\hat{\rho}$, ρ	density of the gas mixture	$\mathrm{kg\,m^{-3}}$, –
τ	non-dimensional time	–
Φ_ζ	shear stress	Pa
Φ	cost function	$\mathrm{cycle^{-1}}$
Π_α	characteristic function of τ and $\Delta\tau_\alpha$	–
$\hat{\omega}_\alpha$, ω_α	mass fraction of gaseous species	–, –

Subscripts and superscripts

$\hat{}$	nominal state and algebraic variables
0	initial value
α, β	gaseous species indices
i	surface reaction index
κ	surface species index
$\mathscr{A}$	state and algebraic variables in *Reactor* $\mathscr{A}$
$\mathscr{B}$	state and algebraic variables in *Reactor* $\mathscr{B}$
STP	state variable at STP
s	solid

References

Aarik, J., Aidla, A., Kasikov, A., Mändar, H., Rammula, R., Sammelselg, V., 2006. Influence of carrier gas pressure and flow rate on atomic layer deposition of HfO_2 and ZrO_2 thin films. Applied Surface Science 252 (16), 5723–5734.

Adomaitis, R. A., 2010. Development of a multiscale model for an atomic layer deposition process. Journal of Crystal Growth 312 (8), 1449–1452.

Åkesson, J., 2008. Optimica—An Extension of Modelica Supporting Dynamic Optimization. In: 6th International Modelica Conference 2008. Modelica Association.

Åkesson, J., Årzén, K.-E., Gäfvert, M., Bergdahl, T., Tummescheit, H., 2010. Modeling and optimization with Optimica and JModelica.org—Languages and tools for solving large-scale dynamic optimization problems. Computers & Chemical Engineering 34 (11), 1737–1749.

Andersson, J., Åkesson, J., Diehl, M., 2012. CasADi: A Symbolic Package for Automatic Differentiation and Optimal Control. In: Forth, S., Hovland, P., Phipps, E., Utke, J., Walther, A. (Eds.), Recent Advances in Algorithmic Differentiation. Vol. 87 of Lecture Notes in Computational Science and Engineering. Springer Berlin Heidelberg, pp. 297–307.

Baunemann, A., 2006. Precursor chemistry of Tantalum and Niobium nitride for MOCVD and ALD applications. Ph.D. thesis, Ruhr-University, Bochum.

Biegler, L. T., 2010. Nonlinear Programming: Concepts, Algorithms, and Applications to Chemical Processes. Society for Industrial Mathematics, PA, USA.

Bird, R. B., Stewart, W. E., Lightfoot, E. N., 1960. Transport Phenomena, 2nd Edition. John Wiley & Sons, Inc., New York.

Blochwitz, T., Otter, M., Arnold, M., Bausch, C., Clau, C., Elmqvist, H., Junghanns, A., Mauss, J., Monteiro, M., Neidhold, T., Neumerkel, D., Olsson,

H., Peetz, J.-V., Wolf, S., March 2011. The Functional Mockup Interface for tool independent exchange of simulation models. In: Proceedings of the 8th International Modelica Conference. Dresden, Germany.

Cleveland, E. R., Henn-Lecordier, L., Rubloff, G. W., 2012. Role of surface intermediates in enhanced, uniform growth rates of TiO_2 atomic layer deposition thin films using titanium tetraisopropoxide and ozone. Journal of Vacuum Science & Technology A 30 (1), 01A150.

Dam, C. E. C., Bohnen, T., Kleijn, C. R., Hageman, P. R., Larsen, P. K., 2007. Scaling up a horizontal HVPE reactor. Surface and Coatings Technology 201 (22–23), 8878–8883.

Davis, M. E., 1984. Numerical Methods and Modeling for Chemical Engineers, 1st Edition. John Wiley & Sons, Inc., New York.

Deminsky, M., Knizhnik, A., Belov, I., Umanskii, S., Rykova, E., Bagatur'yants, A., et al., 2004. Mechanism and kinetics of thin zirconium and hafnium oxide film growth in an ALD reactor. Surface Science 549 (1), 67–86.

Elam, J. W., George, S. M., 2003. Growth of ZnO/Al_2O_3 alloy films using atomic layer deposition techniques. Chemistry of Materials 15 (4), 1020–1028.

Elers, K. E., Blomberg, T., Peussa, M., Aitchison, B., Haukka, S., Marcus, S., 2006. Film uniformity in atomic layer deposition. Chemical Vapor Deposition 12 (1), 13–24.

Elliott, S. D., 2012. Atomic-scale simulation of ALD chemistry. Semiconductor Science and Technology 27 (7), 074008.

George, S. M., 2010. Atomic layer deposition: An overview. Chemical Reviews 110 (1), 111–131.

Granneman, E., Fischer, P., Pierreux, D., Terhorst, H., Zagwijn, P., 2007. Batch ALD: Characteristics, comparison with single wafer ALD, and examples. Surface and Coatings Technology 201 (22-23), 8899–8907.

Henn-Lecordier, L., Anderle, M., Robertson, E., Rubloff, G. W., 2011. Impact of parasitic reactions on wafer-scale uniformity in water-based and ozone-based atomic layer deposition. Journal of Vacuum Science & Technology A 29 (5), 051509.

Hindmarsh, A. C., Brown, P. N., Grant, K. E., Lee, S. L., Serban, R., Shumaker, D. E., et al., 2005. SUNDIALS: Suite of nonlinear and differential/algebraic equation solvers. ACM Transactions on Mathematical Software 31 (3), 363–396.

Hirschfelder, J. O., Curtiss, C. F., Bird, R. B., 1964. Molecular Theory of Gases and Liquids, 2nd Edition. John Wiley & Sons, Inc., New York.

Holmqvist, A., Törndahl, T., Stenström, S., 2012. A model-based methodology for the analysis and design of atomic layer deposition processes—Part I: Mechanistic modelling of continuous flow reactors. Chemical Engineering Science 81, 260–272.

Holmqvist, A., Törndahl, T., Stenström, S., 2013a. A model-based methodology for the analysis and design of atomic layer deposition processes—Part II: Experimental validation and mechanistic analysis. Chemical Engineering Science 94, 316–329.

Holmqvist, A., Törndahl, T., Stenström, S., 2013b. A model-based methodology for the analysis and design of atomic layer deposition processes—Part III: Constrained multi-mbjective optimization. Chemical Engineering Science 96, 71–86.

Jur, J. S., Parsons, G. N., 2011. Atomic layer deposition of Al_2O_3 and ZnO at atmospheric pressure in a flow tube reactor. ACS Applied Materials & Interfaces 3 (2), 299–308.

Knoops, H. C. M., Elam, J. W., Libera, J. A., Kessels, W. M. M., 2011. Surface loss in ozone-based atomic layer deposition processes. Chemistry of Materials 23 (9), 2381–2387.

Levy, D. H., Nelson, S. F., 2012. Thin-film electronics by atomic layer deposition. Journal of Vacuum Science & Technology A 30 (1), 018501.

Magnusson, F., Åkesson, J., Sep 2012. Collocation methods for optimization in a Modelica environment. In: 9th International Modelica Conference. Munich, Germany.

Masel, R. I., 1996. Principle of Adsorption and Reaction on Solid Surface, 1st Edition. John Wiley & Sons, Inc., New York.

Matero, R., Rahtu, A., Ritala, M., Leskelä, M., Sajavaara, T., 2000. Effect of water dose on the atomic layer deposition rate of oxide thin films. Thin Solid Films 368 (1), 1–7.

Miikkulainen, V., Leskelä, M., Ritala, M., Puurunen, R. L., 2013. Crystallinity of inorganic films grown by atomic layer deposition: Overview and general trends. Journal of Applied Physics 113 (2), 021301.

Mousa, M. B. M., Oldham, C. J., Jur, J. S., Parsons, G. N., 2012. Effect of temperature and gas velocity on growth per cycle during Al_2O_3 and ZnO atomic layer deposition at atmospheric pressure. Journal of Vacuum Science & Technology A 30 (1), 01A155.

Puurunen, R. L., 2005. Surface chemistry of atomic layer deposition: A case study for the trimethylaluminum/water process. Journal of Applied Physics 97 (12), 121301.

Rahtu, A., Alaranta, T., Ritala, M., 2001. In situ quartz crystal microbalance and quadrupole mass spectrometry studies of atomic layer deposition of aluminum oxide from trimethylaluminum and water. Langmuir 17 (21), 6506–6509.

Reid, R. C., Prausnitz, J. M., Poling, B. E., 1988. The Properties of Gases and Liquids, 4th Edition. McGraw-Hill, New York.

Ren, J., 2009. Initial growth mechanism of atomic layer deposition of ZnO on the hydroxylated Si(100)-2×1: A density functional theory study. Applied Surface Science 255 (11), 5742–5745.

Ritala, M., Leskelä, M., 2002. Handbook of Thin Film Materials. Vol. 1. Academic Press, New York.

Schiesser, W. E., 1991. The Numerical Method of Lines: Integration of Partial Differential Equations, 1st Edition. Academic Press, San Diago.

Sundaram, G. M., Bertuch, A., Bhatia, R., Coutu, R., Dalberth, M. J., Deguns, E., et al., 2010. Large format atomic layer deposition. ECS Transactions 33 (2), 429–440.

Suntola, T., 1992. Atomic layer epitaxy. Thin Solid Films 216 (1), 84–89.

The Modelica Association, 2012. The Modelica Association Home Page. `http://www.modelica.org`.

Travis, C. D., Adomaitis, R. A., 2013a. Dynamic modeling for the design and cyclic operation of an atomic layer deposition (ALD) reactor. Processes 1 (2), 128–152.

Travis, C. D., Adomaitis, R. A., 2013b. Modeling ALD surface reaction and process dynamics using absolute reaction rate theory. Chemical Vapor Deposition 19, 1–11.

Travis, C. D., Adomaitis, R. A., 2013c. Modeling alumina atomic layer deposition reaction kinetics during the trimethylaluminum exposure. Theoretical Chemistry Accounts 133 (1), 1–11.

Wächter, A., Biegler, L. T., 2006. On the implementation of an interior-point filter line-search algorithm for large-scale nonlinear programming. Mathematical Programming 106 (1), 25–57.

Wilke, C. R., 1950. A viscosity equation for gas mixtures. Journal of Chemical Physics 18 (4), 517–519.

1151 Yanguas-Gil, A., Elam, J. W., 2012. Simple model for atomic layer deposition
1152 precursor reaction and transport in a viscous-flow tubular reactor. Journal of
1153 Vacuum Science & Technology A 30 (1), 01A159.

1154 Yanguas-Gil, A., Elam, J. W., 2014. Analytic expressions for atomic layer depo-
1155 sition: Coverage, throughput, and materials utilization in cross-flow, particle
1156 coating, and spatial atomic layer deposition. Journal of Vacuum Science &
1157 Technology A 32 (3), 031504.

1158 Ylilammi, M., 1995. Mass transport in atomic layer deposition carrier gas reac-
1159 tors. Journal of The Electrochemical Society 142 (7), 2474–2479.

1160 Yousfi, E. B., Fouache, J., Lincot, D., 2000. Study of atomic layer epitaxy of
1161 zinc oxide by in-situ quartz crystal microgravimetry. Applied Surface Science
1162 153 (4), 223–234.